Synthesis and characterization of gallium oxide nanocrystals

Master's thesis
University of Turku
Physics
2022
Kari Iltanen
Examiners:
DSc Pekka Laukkanen
MSc Zahra Jahanshah Rad

The originality of this thesis has been checked in accordance with the University of Turku quality assurance system using Turnitin Originality Check service.

UNIVERSITY OF TURKU
Department of Physics and Astronomy

Iltanen, Kari Synthesis and characterization of gallium oxide nanocrystals

Master's thesis, 62 pp.
Physics
June 2022

In this thesis a method for synthesizing gallium oxide nanocrystals was investigated. This is a new technique and therefore its properties are not well known. By utilizing this method, synthesis of gallium oxide nanocrystals by placing GaAs substrate into hot water is simpler than other methods used so far.

Theory of nanocrystal growth is used to understand what processes are involved in the synthesis. The theory of crystal growth is divided into classical and non-classical parts, where former involves monomer by monomer addition and latter involves intra- and interparticle interactions. This includes interaction between water and substrate and other reactions that could be involved in the synthesis.

Gallium oxide nanocrystals have many applications in optoelectronics and power electronics due to its ultra wide bandgap, high breakthrough voltage and chemical inertness. Some potential applications are deep UV photodetectors, photocatalysis and sensors.

In the experimental part, the first step was to determine properties of nanocrystals synthesized with no additional treatment to establish a baseline, which later samples will be compared to. Later pretreated substrates were used to see how changes in the surface properties of the substrate could have affected the end result of the synthesis.

One of the goals was to find ways to control size distribution and amount of nanocrystals per unit area. For this purpose multiple pre-synthesis treatments for the substrate were tested, such as roughening and seeding. Surface roughness was investigated by atomic force microscopy. Elemental analysis with X-ray photoelectron spectroscopy and electron energy dispersive spectroscopy was used as needed to determine elemental composition of some features and surfaces.

Synthesized nanocrystals were measured with scanning electron microscope (SEM). For each sample size distribution, morphology, fraction of the surface covered by nanocrystals were determined. Most synthesized nanocrystals were quite wide, around seven hundred nanometres, but one modification to the synthesis process reduced the widths of typical nanocrystals by tens of percent. Typical aspect ratios were between five and ten. X-ray diffraction was used to investigate crystal structure of the nanocrystals before and after ultra high vacuum heating.

Keywords: nanocrystals, GaAs, characterization, synthesis, gallium oxide, GaOOH

Contents

Preface

Gallium oxide is a wide bandgap (4,9 eV) semiconductor and therefore transparent in visible light. Its ability to tolerate harsh environmental conditions is significant plus for already attractive material. Interest towards gallium oxide has increased rapidly during the last two decades with most researchers focusing on nanomaterial form. [1]

Due to many potential applications of gallium oxide nanomaterials simple and relatively cheap synthesis methods with good control over product morphology and size distribution, while giving a high purity product, are needed. [1, 2]

Nanomaterials can be prepared with top-down or bottom-up-methods, in the former the starting point is a macroscopic piece which is processed until at least of one of the dimensions is below 100 nm. In the latter, the starting point is different molecules that will combine to form nanoscale features during processing. Due to lower production cost, simplicity, and flexibility bottom-up methods are favoured. However, milling is often used top-down method for nanoparticle preparation. [3]

The synthesized nanomaterials can be in form of quantum dots, nanowires, nanosheets, or nanoparticles depending on desired application and material in question. Whether products are monocrystalline, polycrystalline or amorphous depends on fabrication processes used and material in question. [2, 3]

Many groups have reported the synthesis of gallium oxide nanocrystals by using wet or dry methods, usually wet chemistry using solution based precursors was chosen though vapour phase processes have also been used. [2, 4, 5]

Many dry methods for gallium oxide nanomaterial fabrication require very high temperatures, produce low quality/purity material, have issues with size/morphology control, or use toxic gasses. These include for example thermal evaporation, molecular beam epitaxy, vapour-liquid-solid (VLS) mechanism, arc-discharge, and chemical vapour deposition (CVD). [6]

The bottom-up processes can be divided at least to the following categories: self-assembly, solution based processes, vapour-phase processes. Methods that combine aspects of two latter categories also exist such as aerosol processes. [3]

In the solution processes, the precursors are mixed in solution containing appropriate solvent and possibly other chemicals, increased pressure and high temperatures (up to hundreds degrees Celcius) are typically used. Synthesized nanoparticles can be either deposited on substrate, placed in the solution or separated later from colloidal solution. [3]

Solution based methods are usually easily scalable and lend themselves to batch processing, which allows processing multiple substrates simultaneously. However, product purity and controlling size distribution can be issues. [3, 6]

In solvothermal methods reactants are dissolved into non-aqueous solvent which is then enclosed in the reactor and temperature is increased up to 200 °C often for somewhere 12–24 h. If water is used, then the process is known as hydrothermal. Sol-gel process is typically done in colloidal solutions below 100 °C. [7]

Water was typically used as solvent and often used gallium source is $Ga(NO_3)_3$. Another potential route is based on $GaCl_3$ and either aqueous metal hydroxide or ammonia solution. Some other reported starting points are Ga_2O_3 powder or metallic gallium. [2, 4, 5, 8–10]

In the semiconductor field, individual nanoparticles has to be combined to larger structure for use leading to the challenge of ensuring that these nanoparticles/wires are in correct positions which is under ongoing research. One possible approach is to synthesize nanomaterial directly to substrate and then use traditional microfabrication methods to produce devices. [11]

This work focuses on synthesis, characterization and applications of Ga_2O_3/GaOOH nanocrystals produced by immersing GaAs piece into hot water, which is a recently developed synthesis method. Some major questions are controlling the size distribu-

tion of produced nanocrystals, their density on the substrate and growth mechanism.

Table I gives a brief comparison of various methods used to synthesize Ga_2O_3 nanoparticles and shows that hydrothermal methods are a good choice when looking a generic synthesis method, which is simple and cheap while providing a good quality product.

Table I. Advantages and disadvantages of β-Ga2O3 NWs growth techniques as given by Alhalaili *et al.* [6].

Growth Mechanisms	Advantages	Disadvantages
Thermal oxidation	Simple, inexpensive	Low degree of control
Vapor–liquid–solid	Good control of growth	Can interfere with doping levels
Pulsed laser deposition	High deposition rate	More defects and dislocations
RF sputtering	Non-stoichiometric growth	Gas incorporation, low quality NWs
Thermal evaporation	Inexpensive, many materials	Contamination
Molecular beam epitaxy	High growth rate, low impurity levels	Rougher surface at higher temperatures
Laser ablation	High quality film	Expensive, require longer time
Arc-discharge	Fast growth	Low quality NWs, many defects
Carbothermal reduction	Simple, variety of structures	High levels of impurities
Microwave plasma	Variety of nanowires	Radial nonuniformity
MOCVD	High growth rate	Expensive, uses toxic gases
Hydrothermal method	Simple, cheap and efficient	Require precise temperature control
Sol-gel method	Simple, inexpensive	nonuniform thickness

The chosen synthesis method in this work holds advantage over many other wet chemistry based methods where the synthesis is done in either base or acid solution and the end is nanocrystals in the solution. The major challenge compared with other methods is the need to harvest the nanocrystals from the growth substrate.

1 Theory

In this chapter nanocrystal growth mechanisms in solution are introduced, along with processes involved in the chosen synthesis method, before moving to nanocrystal properties and applications.

1.1 Crystal growth in solution

Growth of bulk crystal happens when chemical potential of the crystalline phase (μ_c) is lower than that of the growth medium (μ_m), as stated by laws of thermodynamics. At the start of the nucleation process, the amount of surface/interface atoms is a significant factor as they supply the energy needed for the crystal growth. After the crystal has grown large enough the contribution of interface energies can be ignored and the bulk free energies of each phase is used. [12, 13]

The chemical potential (μ) and free energy (G) are connected to each other through equation (1), where S is entropy, and N_i is the number of particles of species i, with V, P and T being volume, pressure and temperature respectively.

$$\mathrm{d}G = -S\,\mathrm{d}T + V\,\mathrm{d}P + \sum_{i=1}^{n} \mu_i\,\mathrm{d}N_i \tag{1}$$

Equation (2) gives the formula for $\Delta\mu$ in solution, where k_B is the Boltzmann constant, C the actual solute concentration and C_e the concentration of saturated solution. By using the level of supersaturation $\sigma = (C - C_e)/C_e$, equation (2) shows approximately direct proportionality to σ. [12]

$$\Delta\mu = \mu_m - \mu_c = k_B T \log(C/C_e) \approx k_B T \sigma \tag{2}$$

Three different processes involved in the crystal growth are interface kinetics, volume diffusion, and removal of latent heat generated. The interface kinetics introduces atoms and molecules into the crystal phase through the interface between the crystals and the growth medium. [12]

In volume diffusion atoms and molecules diffuse from the growth medium to the growth interface with rate proportional $\beta_{st}[C(a) - C_e]$, where β_{st} is the rate constant and $C(a)$ is the concentration on radius a (lattice constant) from spot on the surface. The free energy difference between crystal and growth medium is released as heat, which has to be removed. [12, 14]

The movement of molecules from solution to the growth site is thought to happen in multiple steps instead of volume diffusion directly to the site as activation energy for desolvation is much larger than activation energy for volume diffusion. [12, 15]

The process starts with the adsorption of molecules to the crystal surface followed by surface diffusion to the growth site and attaching to the crystal. This leads to smaller activation energies for each step, while total activation energy remains the same. Figure 1 illustrates energy levels involved in previously described processes. [12, 15]

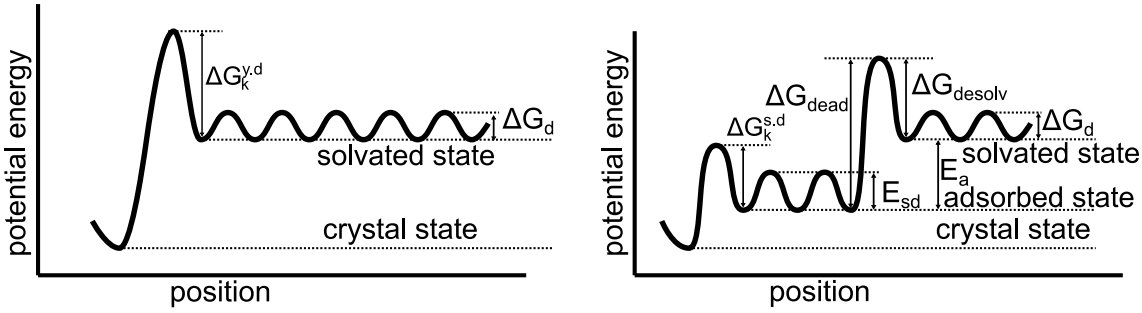

Figure 1. On the left a diagram showing energy levels for direct solvation of crystal. On the right desolvation of crystal through intermediate adsorbed state. Diagrams modelled after Figure 2.16 at [12].

Nucleation theory is divided into classical and non-classical theories, the former considers the nucleation process though a monomer-by-monomer addition which does not hold true for nanoscale processes. The non-classical growth is a much more complex process as it involves the aggregation of smaller particles into larger ones, prenucleation clusters, and particle assembly pathways. [13, 15]

Pre-nucleation clusters form crystal nuclei through intermediate liquid-like intermediate and amorphous phases acting as intermediate steps. The liquid-like phase

consists of one phase with the high concentration of cluster molecules and other with low concentration. The size of the first phase increases through the diffusion of cluster molecules from area with lower concentration driven by free energy difference. Then as the degree of supersaturation increases a solid particle eventually forms from area with high concentration. [15, 16]

Assembly by primary particles involves a subcritical nucleus that is unstable and tends to dissolve. However, if the collision rate is higher than dissolution rate two or more subcritical nuclei can merge forming stable postcritical nuclei. The low supersaturation degree and high concentration of subcritical nuclei favour this process. [14, 15]

Other nucleation processes are cluster-cloud mediated nucleation and multistep nucleation in solid-solid transitions. In the former process relatively stable clusters within a cloud form poorly crystalline nanoparticles with a cluster-cloud structure, which matures to a well-crystallized one through relaxation involving matter exchange with the cloud. In the latter process, an intermediate liquid stage is involved in transition from the initial nucleus to a stable nucleus with final lattice type. [15]

1.1.1 Nanocrystal growth

In aqueous synthesis, at least four major parameters are important, the solubility product of semiconductor compounds in water, the binding affinities of particle surface capping ligands, water/hydroxyl ions for the metals, and pH of the aqueous media. The hard and soft acids and bases theory provides a qualitative explanation for the role of above thermodynamic parameters. [17]

The chemical basis of the aqueous synthesis is Lewis acid/base reactions usually involving H^+, OH^-, O^{2-}, and H_2O. In Lewis acid/base reaction the base donates a pair of electrons and acid receives them. [17, 18]

The exact growth mechanisms and impact of process conditions depend on the

chosen synthesis method, but for processes in aqueous solutions the concentration of hydroxide ions play significant role on the morphology and size of product. The amount of OH^- ions forming coordination complex with Ga^{3+} ion increases with pH. [9]

Differences in the free energies of the facets cause differences in formation of active sites and the growth rate. Increase in the free energy increases growth rate and the end result is anisotropical growth. [9]

The classical LaMer model recognizes three stages of particle formation: monomer accumulation, nucleation, and growth (Figure 2). Particle size distribution stays narrow if burst nucleation is made possible though the system favouring quick monomer accumulation. Slow growth rate during the growth stage favours narrow size distribution or retaining it. [7, 14, 17]

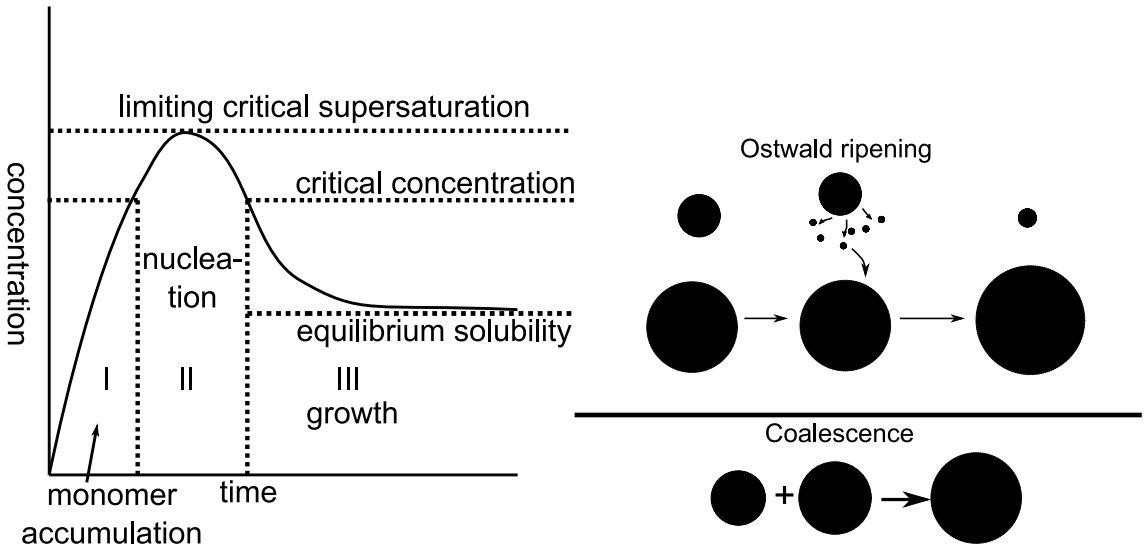

Figure 2. On the left LaMer diagram showing the stages of formation, modelled after figure 12 in [18]. On the right diagrams for Ostwald ripening and coalescence, modelled after diagram of Ostwald ripening in Wikimedia Commons.

The growth rate can depend on either from the flux of monomers to the particle or precipitation and dissolution of monomers. The former is known as diffusion controlled growth model and latter as surface reaction controlled growth model. [14, 17, 18]

As the nucleus has a high surface-to-volume ratio the thermodynamic energy barrier is high, which prevents the random formation of particles leading to the short bursts of nucleation under high supersaturation. [19]

Formation of nanoclusters with discrete sizes and structures during prenucleation period is a well-known effect caused by local energy minima which would lower the nucleation energy barrier. These clusters can be stabilized by geometric full-shell and electronic superatom configurations or by other structural properties. Some contributions to the nonclassical nucleation pathway come from structural variances, such as amorphism and polymorphism. [19]

In some cases, the nucleation is a two-step process starting with formation of amorphous nuclei before crystallization starts in the middle of the amorphous phase. This lowers the free energy barrier of crystallization as the surface energy of amorphous nuclei is lower than crystalline nuclei due disordered solution-nuclei interfaces. Amorphous layer buffers the large entropy differences between solution and crystalline phase. [19, 20]

Major part of the growth process is the interaction of the nanoparticles in the solution with each other, which often determines the morphology and size distribution of the synthesised nanoparticles. In agglomeration weakly bonded particles form an assembly. [7, 21]

In oriented attachment (OA) free energy between two nanoparticles is minimized through the surface energy reduction of the two-nanoparticle system which happens when nanoparticles adhere to the crystal plane with the highest surface energy or maximum surface area. The bonding and interfacial energy is minimized when particles are oriented in the same crystallographic direction as they attach to each other, which requires particles to rotate. [15]

While the alignment tendency in OA is strong, some specific misalignments are energetically favoured at the grain boundary of interparticle interface. Surface lig-

ands on nanoparticles can prevent attachment requiring ligand removal, to which the mass transport of atoms during merging potentially contributes. [19]

When the individual nanoparticles bond strongly to each other with the resulting particle having much smaller surface area than sum individual surface areas, the process is known as aggregation. [7, 21]

Random aggregation is another crystallization by particle attachment pathway, resulting in the creation of polycrystals when crystalline nanoparticles randomly adhere to each other and fuse together. [14, 15]

In coalescence, the total surface area decreases as aggregates link together resulting in the end of the aggregation process forming a coarser domain from two-phase domains coming to contact each other. [21]

Ostwald ripening is a particle growth mechanism favouring growth of coarse particles at the expense of fine particles. This is caused by the redistribution of atoms between fine and coarse particles as atoms desorbing from fine particles attach to coarse particles. The inverse process, known as digestive ripening, involves the movement of atoms from larger particles to smaller ones. [7, 14, 21]

$$\frac{\mathrm{d}r}{\mathrm{d}t} = \frac{K_D}{r}\left(\frac{1}{r^*} - \frac{1}{r}\right),\ K_D = \frac{2\gamma D v^2 C_b}{k_B T} \tag{3}$$

Equation (3), where r^* is the particle radius in equilibrium within the bulk solution, γ the surface energy, D the diffusion coefficient, v the molar volume, C_b the bulk concentration of monomers within the solution and k_B the Boltzmann constant, describes the rate particle size change during Ostwald ripening. [14]

For narrow size distributions the (3) can be rewritten to (4), $\bar{r}$ is the mean particle radius and Δr the change in the standard deviation. The level of supersaturation determines whether the size distribution narrows ($\bar{r}/r^* >= 2$) or broadens ($\bar{r}/r^* < 2$) during growth. In the latter case broadening is likely even for diffusion controlled growth. [14]

$$\frac{\mathrm{d}\Delta r}{\mathrm{d}t} = \frac{K_D \Delta r}{\bar{r}^2}\left(\frac{2}{\bar{r}} - \frac{1}{r^*}\right) \tag{4}$$

For surface reaction controlled growth the equivalent equation set to (3)-(4) are (5)-(6), where k is the rate constant for surface reaction and R the molar gas constant. In this case the size distribution always broadens.[14]

$$\frac{\mathrm{d}r}{\mathrm{d}t} = \frac{K_R}{r}\left(\frac{1}{r^*} - \frac{1}{r}\right),\ K_R = \frac{2\gamma k v^2 C_b}{RT} \tag{5}$$

$$\frac{\mathrm{d}\Delta r}{\mathrm{d}t} = \frac{K_R \Delta r}{\bar{r}^2} \tag{6}$$

In some cases particle size distribution is bimodal, which is possible though aggregation. The distribution peaks would correspond with primary nanocrystals and the aggregate growth product. The primary crystals correspond with the critical size of crystals, which is smaller than aggregated particles. Pre-existing bimodal distributions can be accentuated by Ostwald ripening, but not caused by it. [13]

Spinodal decomposition model has no practical energy barrier and bulk free energy significantly higher than surface energy allowing the latter to be ignored. This leads to spontaneously occurring spinodal decomposition meaning that phase separation happens everywhere in the reaction medium. [19]

Whether particle growth is controlled by diffusion or surface reaction affects the development of the size distribution and the speed of the development. In the former, the growth rate depends on surface area of the particle and in the latter the monomer flux. Other processes involved in the growth, such as aggregation or Ostwald ripening can lead to the broadening of the size distribution. [7, 18]

In the diffusion controlled process, the self-focusing phenomena can cause smaller particles to grow faster. One factor in anisotropic growth is the selective binding of two or more ligands to the different facets or varying affinity of single ligand species for different facets. In large enough particles diffusion can not maintain the

same concentration all over the particle and concentration gradients form around the particle as reactions on some facets are faster than in others. The concentration differences even out the differences on reaction speed leading to more isotropic growth. [7, 18]

In diffusion limited aggregation, the rate of particle and aggregate collisions determines the aggregation rate. Fractal structures form if particles attach rigidly to the aggregates preventing restructuration of the aggregate. For the low attachment probabilities of the particle to the aggregate, the process is classified as reaction limited, which produces denser and more stable structures. [7]

If the crystal facets of nanoparticles have higher free energy than monomers in the solution, no net growth happens but monomers can diffuse along the surface, which changes the shape of the particle. Differences between the surface free energies of different facets lead this intraparticle diffusion where high energy facets dissolve. [14]

1.1.2 Reactions

Speed of chemical reactions has an exponential temperature dependence ($\exp -E_a/RT$), where E_a is the activation energy. Reaction can not happen if reagent molecules do not have enough energy to overcome an energy barrier known as activation energy. Self-ionization (dissociation) of water leads to the low concentration of hydroxide and hydronium ions in solution, which increase with the temperature at normal pressure. Solubility also changes with the temperature. [22]

The adsorption of water to GaAs surface is the first part of the synthesis reaction path and it can then diffuse deeper into the substrate. Water can be chemically adsorbed either as individual molecules or dissociated form through both processes might also be present. If adsorption is physical, then water molecules attach to surface with van der Waals forces. [23–25]

Exposure of GaAs to liquid water results in growth of gallium oxide to the surface, which has lower solubility than As oxide, resulting in the faster removal of the latter. Formation of $Ga(OH)_3$ and H_3AsO_3 is another possibility mentioned in the literature, with latter dissolving freely while the dissolution of gallium hydroxide depends on concentration of Ga^{3+} ions in the solution. Unless running water is used the result is arsenic depleted layers on GaAs as increasing Ga^{3+} concentration prevents gallium hydroxide dissolution. [24, 25]

Following reactions $Ga(OH)_3 \longrightarrow GaOOH + H_2O$ and $2\,GaOOH \longrightarrow Ga_2O_3 + H_2O$ offer paths to GaOOH and Ga_2O_3. [26, 27]

GaAs has a zinc blende crystal structure with the lattice constant being 565,315 pm and therefore has a lattice mismatch with Ga_2O_3 and GaOOH. This mismatch can cause defects or structural and morphological disorder. Formation of different polymorph or even polycrystalline material is another possibility. [6]

The substrate crystal direction can also affect the growth interatomic distances on crystal planes depend on the direction of the normal of the plane. When combined with different crystal planes of the growth, lattice mismatch can be often reduced. However, if the crystal structure of the product is completely different from substrate's large mismatch is likely happen even if the crystal plane of the substrate surface is chosen so that mismatch is reduced. [6]

1.2 Nanocrystal properties

Gallium oxide has a very high melting point, excellent structural stability and excellent chemical resistance at very high temperatures (above 1000 °C). These factors make it attractive device material especially for harsh environments. [6, 26, 28]

GaOOH has an orthorhombic lattice and can be transformed to pure oxide with calcination. Ga_2O_3 on the other hand has five different crystal structures (polymorphs) that exists in overlapping pressure and temperature ranges. Usually Ga_2O_3

is the β-variant as it is the most stable form, and has monoclinic lattice crystal structure. All other phases are metastable changing to β-variant at temperatures above 600 °C. Figure 3 shows different polymorphs and transformations between them, along with the crystal structure of GaOOH. [6, 29, 30]

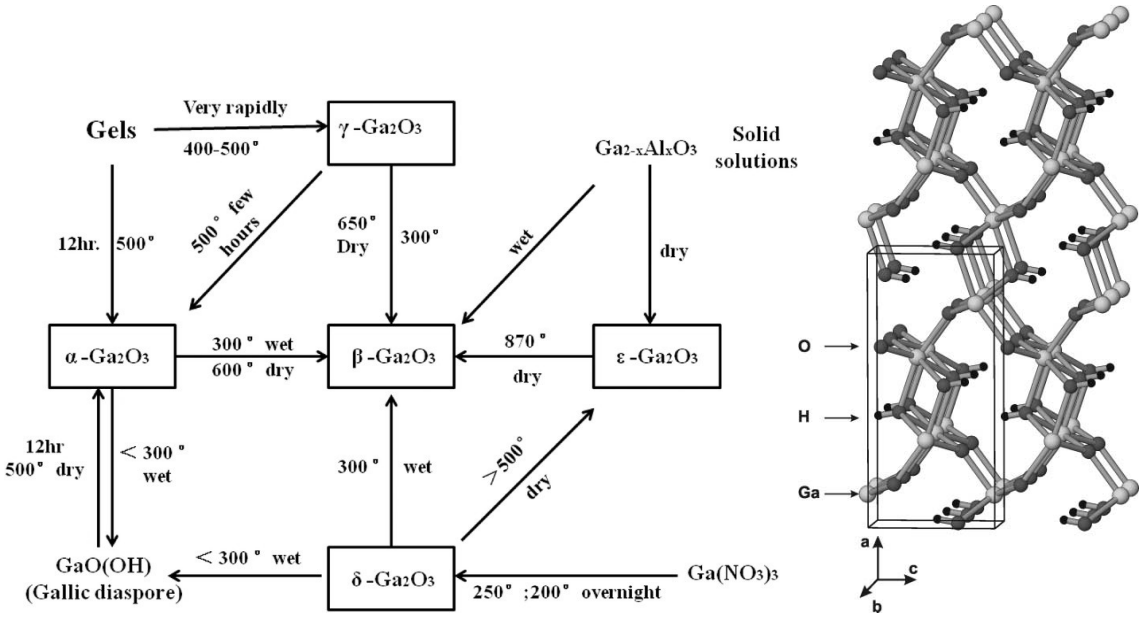

Figure 3. On the left paths for transforms between different gallium oxide polymorphs. Source: Shi and Qiao [26], arrow directions on left switched around. On the right model of GaOOH lattice structure, source Li *et al.* [31]. Note how hydrogen atoms lead to large open spaces in the crystal structure. Licence for both: CC-BY-4.0.

β-Ga_2O_3 unit cell consists of octahedral (GaO_6) and tetrahedral (GaO_4) crystalline structures (Figure 4). The double chain arrangement of GaO_6 octahedra with GaO_4 tetrahedra connecting them along b-axis explains differences in electron mobilities in different directions with the highest along the b-axis direction. [6, 26]

The other polymorphs have cubic defective spinel (γ, Figure 4), rhombohedral, cubic (δ), or orthorhombic (ε) lattices. Different polymorphs have different bandgaps. α-Ga_2O_3 is the second most common polymorph and has rhombohedral lattice (Figure 4), which is also known as corundum. The exact structures of delta and epsilon polymorphs are uncertain as getting them pure is difficult. [1, 26, 30]

The gamma polymorph has defective spinel structures as it has partially occupied

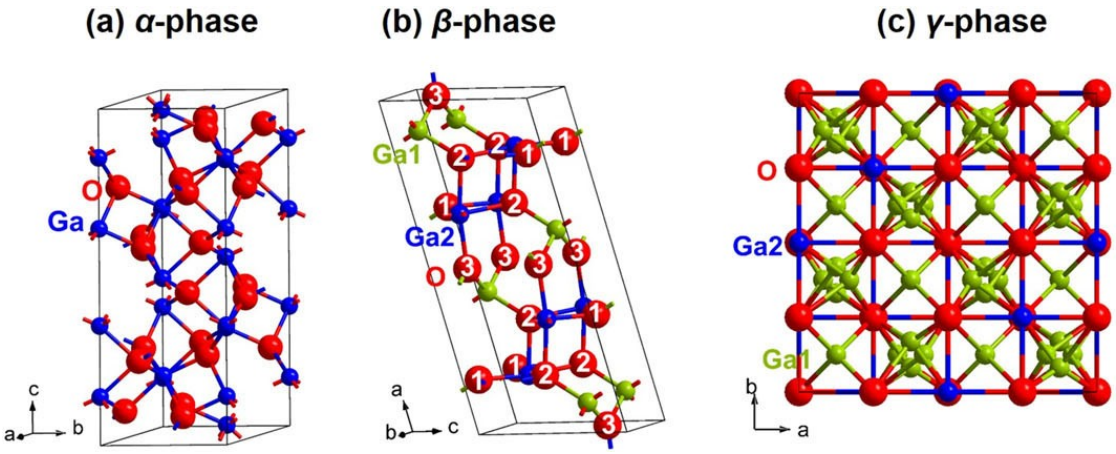

Figure 4. Crystal structures of alpha, beta, and gamma polymorphs of Ga_2O_3. Note that alpha has only a single coordinating Ga site, while beta and gamma have multiple coordinating Ga sites. For gamma polymorph the ratio of green and blue coordination sites is 1:2. Source: Zhang *et al.* [32], image was cropped. Licence: CC-BY-4.0.

gallium sites. Also, some texts mention a kappa polymorph but later research has indicated that it is a nanostructured variant of β-polymorph. Information about the crystal structures of α, β, and γ polymorphs and GaOOH is given at the Table II showing large differences between the lattice parameters. [1, 26, 30]

Table II. Experimentally determined crystal structures of three different gallium oxide polymorphs and GaOOH with corresponding lattice parameters according to Sharma *et al.* [30].

Sample	Crystal type	Lattice parameters (pm, °)
GaOOH	orthorhombic	a=980,16, b=297,49, c=455,31, α=β=γ=90
α-Ga_2O_3	rhombohedral	a=b=498,20, c=1343,7, α=β=90, γ=120
β-Ga_2O_3	monoclinic	a=1221,7, b=303,92, c=580,95, α=γ=90, β=103,81
γ-Ga_2O_3	spinel	a=835, α=β=γ=90

Gallium oxide has poor thermal conductivity compared to other semiconductors. As β-Ga_2O_3 is anisotropic, thermal conductivity depends on the crystallographic orientation of the heat gradient. Both phonon and free electrons appear to restrict conductivity as the material does not show typical $T^{3/2}$-dependency. [26]

As a wide bandgap material Ga_2O_3 requires doping or very high temperatures to show non-insulator conductivity. N-type conductivity is usually attributed to oxygen vacancies, but some researchers have considered the presence of hydrogen as cause or impurities. One of major problems is fabrication of p-type gallium oxide, limiting potential applications for Ga_2O_3 based devices. The breakdown voltages of gallium oxide are also very high. [26]

Oxygen vacancies and extra gallium atoms in the lattice can change electrical characteristics of Ga_2O_3 nanowires. Oxygen vacancies can act as donors and gallium or gallium-oxygen-vacancies as acceptors, also an impurity band exists much deeper in the bandgap. Surfaces of the low Miller index crystal planes of β-Ga_2O_3 always have oxygen vacancies. [2, 26, 33]

Typically, beta-Ga_2O_3 nanostructures have band-to-band and sub-bandgap emissions with latter having blue, green, and red emission bands. The UV emissions from former are caused by the recombination of a self-trapped exciton. These can be explained with donor-acceptor pair (DAP) model, where the donor acts as a trap for the electron excited to the conduction band. The relaxation happens through trapped exciton formation by electron tunneling from the donor to an acceptor and subsequent exciton recombination at the acceptor site. [2, 33]

Luminescent properties of GaOOH differ from Ga_2O_3 possibly due to OH^- vacancies present. [26]

Gamma-Ga_2O_3 nanostructures have size-tunable photoluminescence as smaller nanocrystals have higher intensity in temperatures above 200 K. As nanocrystal size decreases donors bind the electron tighter making it harder for them to get captured by acceptor sites. [34]

Wide photoluminescence bands with no discrete lines are attributed to either strong phonon coupling or a wide distribution of donor and acceptor states. As the capture of a photogenerated hole by surface defects, especially OH^-, competes

with capture by acceptors it quenches the DAP emission. The defects can be eliminated by the chemical modification of the surface, where a ligand replaces functional originally present at the defect site. [34]

For applications gallium oxide and other wide bandgap semiconductors suffer from low conductivity, large dislocation densities and thermal expansion mismatches leading to the cracking of deposited films. Bandgap of Ga_2O_3 could be adjusted by adding other elements, such as In, Er, Zn and Mg, to it in the specific ratio to achieve wanted bandgap value. This practice is known as energy-band engineering. Table III lists some physical and electronic properties of GaOOH, α-Ga_2O_3, and β-Ga_2O_3. [35]

Table III. Material properties of GaOOH, α-Ga_2O_3, and β-Ga_2O_3 according to both Ahmadi and Oshima and Zhang *et al.* [32, 36]. The large variation of mobility values are caused by material quality and carrier concentration.

Property	GaOOH	α-Ga_2O_3	β-Ga_2O_3
density	5,13 g/cm^3	6,18 g/cm^3	5,68 g/cm^3
E_g	4,75 eV	5,3 eV	4,8 eV
E_{br}		9,5 MV/cm	6,5 MV/cm
μ_e		10–200 cm^2/Vs	10–200 cm^2/Vs
ε		10	10
n-type dopant		Si, Ge, Sn	Si, Ge, Sn
p-type dopant		no report	N (deep acceptor 1 eV)

As Ga^{3+}-ion has similar chemical properties as Fe^{3+}-ion due the similar ionic radius, biological systems can take gallium instead of iron. However, gallium ions have no redox activity disturbing cellular respiration which can be lethal to pathologically proliferating cells. [26]

1.3 Applications

Ga_2O_3 nanocrystals can act as photocatalyst. The photocatalytic performance of β-Ga_2O_3 is attributed to the large bandgap, optical properties, reactant absorptivity, and transport rate of photogenerated electron-hole-pairs. [37, 38]

Ali *et al.* have used modified beta-Ga_2O_3 nanorods as photocatalyst for water splitting in visible light. Produced nanorods had cobalt phthalocyanine molecules attached to surface leading to a heterojunction and shifting absorption to longer wavelengths. The used modification increased sonophotoactivity for H_2 evolution about two orders of magnitude compared with pure Ga_2O_3. The high photocatalytic activity is thought to be caused mainly by the suitable energy band position of the modified nanorod and preferable activation capacity for O_2. The modifier has bands at energy levels matching those of bandgap of Ga_2O_3 leading to the modified nanorod with states in whole energy range. [39]

Ga_2O_3 nanocrystals can also act as templates for growing ultralong GaN nanowires, or they could be transformed to coaxial Ga_2O_3/GaN nanowires. Both processes are done at high temperatures, 900–1050 °C or above, to enable ammonia decomposition, which provides nitrogen and hydrogen required for the reactions. [2]

Sivukumar *et al.* have tested a resistive random-access memory device based on single-crystalline β-Ga_2O_3 nanowires grown on silicon substrate with gold catalyst using the vapour liquid solid method. Then nanowires were uniformly dispersed on the substrate surface by exploiting van der Waals force between the surface and the nanowires. Next step was metal electrode, Au/Ti, deposition by using a shadow mask. Only one nanowire intersected the electrode pair. The required changes between two resistivity levels was enabled by oxygen vacancies in the nanowire formed during the synthesis. See Figure 5 for device structure and I-V results. [40]

Tang *et al.* have developed and tested an anode consisting of carbon coated Ga_2O_3 nanoparticles for the lithium ion battery. The synthesis was done hydrother-

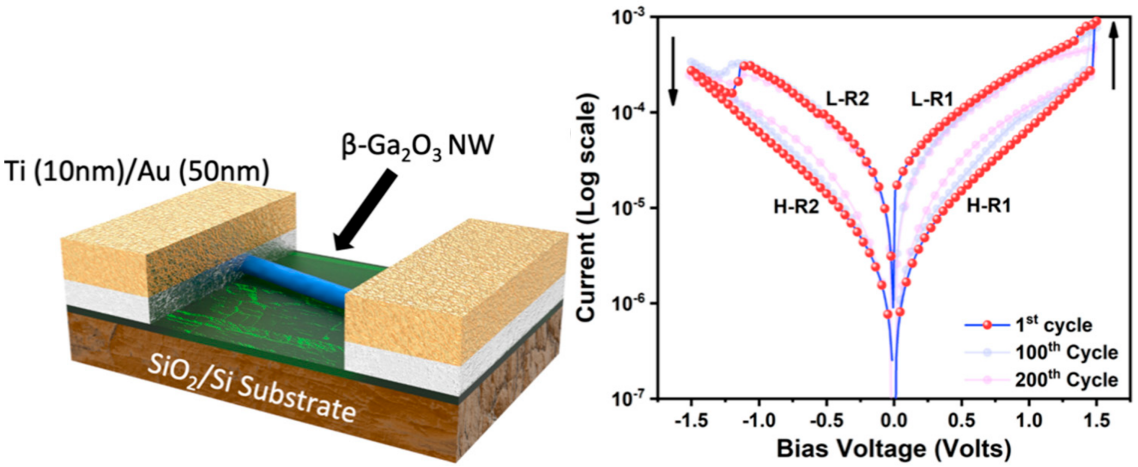

Figure 5. On the left schematic of the tested device. On the right measured voltage-current relationship of the device. Source: Sivakumar *et al.* [40], licence: CC-BY-4.0, cropped from original.

mally, after which the product was calcinated. Their tests showed good performance due the prevention of surface aggregate formation. [41]

According to Das *et al.* β-Ga_2O_3 nanobricks hybridized with reduced graphene oxide, which wraps around the nanobrick, has good field emission characteristics. The turn-on field is lower and emission current higher in the β-Ga_2O_3 than in α-Ga_2O_3 due higher density of large pores leading to larger surface area and more active sites for carrier transfer. [42]

Biomedical applications of gallium oxide nanomaterials show great potential but research on them is in its infancy. Potential use cases include multifunctional drug carriers and an antibacterial agent. [26]

Owing to high breakdown field Ga_2O_3 has potential applications in power electronics, where high voltages are used. [26]

Wang *et al.* have synthesised porous Ga_2O_3 nanoparticles doped with Cr for transporting an antitumour drug. The nanoparticles were coated with a biopolymer to improve targeting and stability. Near-infrared photoluminescence imaging was done to ensure that nanoparticles accumulate to the target. [43]

1.3.1 Sensors

Use of Ga_2O_3 nanowires as gas sensor can be attributed to gas absorption to the surface defects of the nanowire which changes dielectric constant of the nanowire and can be measured though changes in device capacitance. Another possible detection mechanism is chemiresistive, where conductivity changes due to surface reactions with gas molecules. [6, 29]

Chiang *et al.* report of a Ga_2O_3 nanorod based extended-gate field effect transistor for pH sensing. They used a glass substrate with indium tin oxide (ITO) layer on top and then deposited GaOOH nanocrystals from a chemical bath before annealing in a furnace to transform the nanorods to α-Ga_2O_3. Their experiments showed excellent pH sensing ability and good linearity. Change in the gate-source voltage, which was measured, was linearly dependent on pH. [44]

Wang *et al.* have built a humidity sensor from Ga_2O_3 nanorods doped with Na and K synthesised from GaN powder and mixture of potassium and sodium acetates in water/ethyl alcohol solution. The end result was annealed and then mixed with water for spin coating of Al_2O_3 substrate. Humidity was determined from sensor impedance. The sensor adsorbs more water molecules higher the humidity is leading to changes in the conduction processes. Their results show a promising candidate for applications due high sensitivity and reliability. [45]

1.3.2 Optoelectronics

Ga_2O_3 nanowires can be used as UV-photodetectors, especially in 200–280 nm range. Solar radiation in this range is absorbed by the ozone layer, which removes background noise allowing the detection of very weak signals. Wide bandgap material such as Ga_2O_3 are not affected by longer wavelengths. [6]

Zeng *et al.* report of a UV photodetector consisting β-Ga_2O_3 nanowires on GaN substrate. The nanowires were fabricated with MOCVD on square holes etched

to SiN layer, after which a graphene layer was deposited on top as the transparent electrode. Ti/Au lead electrodes were used. In this structure graphene and β-Ga_2O_3 form a p-n junction with the depletion region at the interface. [46]

Test showed detector responsive in wavelengths 230–370 nm with larger value determined by GaN bandgap. Fast response was attributed to good crystal quality. Other performance characteristics were comparable or better than other Ga_2O_3 nanowire device designs. Figure 6 shows the schematic and band diagram of this device. [46]

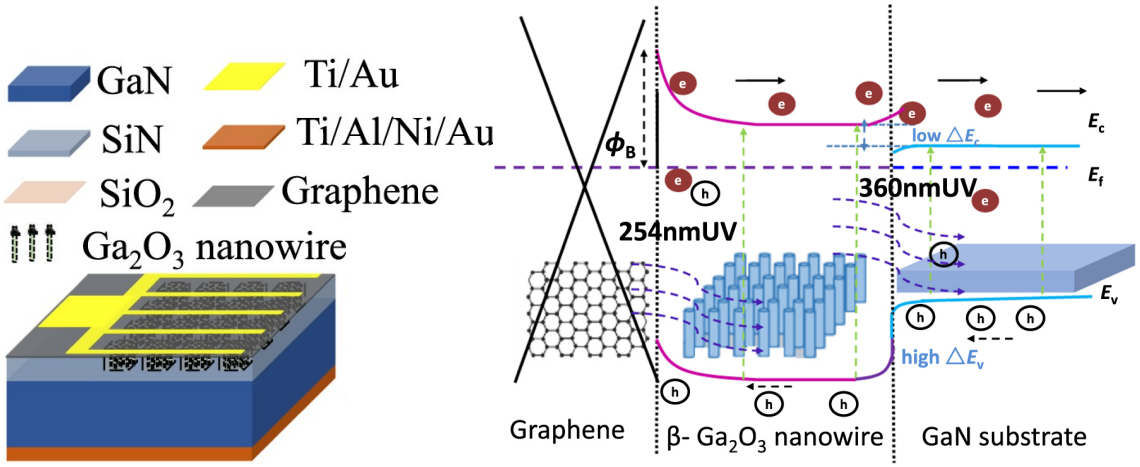

Figure 6. On the left schematic of the tested device. On the right band diagram of the device showing also movements charge carriers and wavelength limits. Source: Zeng *et al.* [46], licence: CC-BY-4.0, cropped from originals.

Ga_2O_3 can be used in electroluminescence devices on the same wavelengths as it has photoluminescence. Some groups have fabricated deep UV LEDs, also incorporation to solar cell structures is possible and some test have been done. [47]

2 Methods

This chapter introduces experimental methods used in synthesis, characterization and both device fabrication and testing.

2.1 Synthesis and harvesting

Before synthesis GaAs samples were cleaned in isopropanol (IPA) in ultrasonic bath and then native oxide was removed in solution consisting of HCl and IPA after which another IPA bath was done. The synthesis itself was done by placing samples into hot water, where nanocrystals form on the substrate surface. After synthesis, the sample was dried with nitrogen. Holding small samples in reaction containers was done with locking tweezers.

Hot plate was used to heat the water and keep it hot. Harvesting nanocrystals from the substrate surface could be done mechanically or chemically. Selectively etching GaAs below nanocrystals to release them to solution and then collecting nanocrystals from the solution was one of tested approaches to harvesting.

Three different pre-synthesis substrate roughening methods were tested: scraping, argon ion sputtering, and chemical roughening. Wang *et al.* have looked into the effects of argon ion sputtering on GaAs surface with ion energies up to 1,2 keV [48].

For chemical roughening ammonia solution was added to hydrogen peroxide solution to raise its pH over 7,5, which Brozel and Stillman say produces rough surface. pH was checked with indicator strip. After etching samples were flushed in a container of water and then put into hot water. [49]

To get Ga_2O_3 nanocrystals the chemically synthesized product has to be heat treated. Sample surface temperature was monitored during heating with a handheld camera with a integrated infrared temperature sensor.

2.2 Characterization

Synthesized nanocrystal were investigated with scanning electron microscopy (SEM) to determine their morphology, size distribution, density and orientation in respect of each other while still on substrate. X-ray diffraction (XRD) was used to investigate the crystal structure of the nanocrystals.

The elemental composition of the samples after synthesis was investigated by using both energy dispersive x-ray spectroscopy (EDS) and x-ray photoelectron spectroscopy (XPS). Both methods can be used to measure the composition of individual spots or with mapping function specified area or pattern. Surface roughness was investigated with atomic force microscopy (AFM).

2.2.1 SEM

In SEM, a sample in the vacuum chamber is scanned with the electron beam and either backscattered (BSE) or secondary electrons (SE) are detected and used to form an image of the sample. Secondary electrons are electrons that incoming electrons kick away from sample atoms, and they have lower energy than backscattered electrons. Therefore, SE provide topographical information as they can only exit the sample close to surface. [50]

Beam energy is usually in range 1–30 keV, but even lower energies are possible. Figure 7 shows a profile of interactions of the electron beam in the sample giving some idea where SE, BSE and X-rays come from. [50]

Backscattered electrons give information about sample composition and topography while secondary electrons are good for imaging structures. However, backscattered electrons generate more secondary electrons with similar energies within the sample and from the chamber than those generated by the incident beam on the surface, which form only small part of total. [50]

The beam energy determines how deep information is gathered, a low energy

beam is good for investigating surface layers of the sample, on the other hand high energy beam is used when investigating deeper structures at cost of lost surface details. [50]

Current SEMs always have multiple detectors installed. Backscattered electrons are usually detected with a semiconductor detector installed to the electron column. Everhart-Thornley detector (ETD) is used for secondary electrons but can also detect backscattered electrons. It consists of a scintillator for optical signal generation and Faraday cage to protect the electron column from large positive potential (>10 kV) of the scintillator and to collect secondary electrons from vicinity with positive potential of a few hundred volts. [50]

As electrons enter to a through-the-lens detector for secondary electrons through the lens it excludes backscattered electrons and secondary electrons generated from the chamber and provides higher resolution though the exclusion of low resolution components. [50]

The semiconductor detector for BSE consists of typically two semicircular segments and can be operated in a sum or difference mode or as an individual detector component. The sum mode provides good compositional contrast compared to ETD image as topographic contrast is suppressed due to the large solid angle of the detector. [50]

In the difference mode topographical contrast is high and compositional contrast low. The subtraction order of individual signals determines whether topographical features are shown correctly as the inversion of subtraction order causes protuberances in the image to become concavities. [50]

2.2.2 EDS

In EDS, the sample is ionized with the electron beam and generated x-rays are analysed to determine sample composition. The x-ray wavelength depends on energy

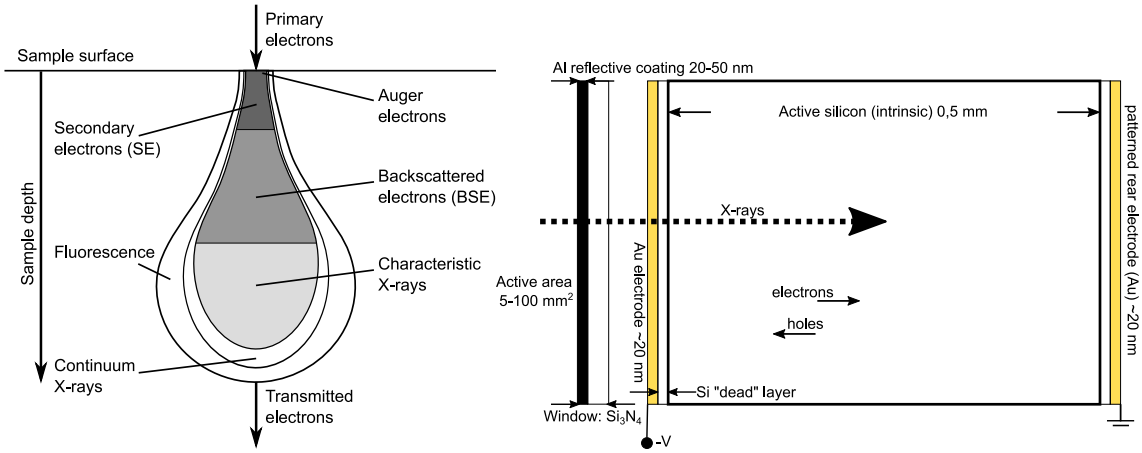

Figure 7. On the left a diagram showing different interactions of electron beam in affected region of sample and depths they happen (Public Domain, Wikimedia Commons). On the right a diagram of EDS detector, based on Figure 16.1 in [50].

difference between empty position and that of the relaxing electron and is characteristic of specific element. [50]

EDS is additional detector in SEM and can only be used to identify elemental composition as it tells nothing about its chemical neighbourhood. Also, the detection of hydrogen and helium is not possible as they do not have x-ray peaks and sensitivity increases towards larger atoms. Measurement depth can be up to a few micrometres with spot sizes typically in micrometre range. [50]

Current silicon drift detectors (Figure 7) used in EDS do not need liquid nitrogen cooling used with previous generation lithium-drifted silicon detectors as Peltier cooling is enough. The active part of the device is layer of intrinsic silicon between biased electrodes where x-ray photons generate holes and electrons. The photon energy is determined from collected charge. Detectable photon energies are typically in range 0,05–30 keV. [50]

Beam energy determines what elements can be detected as it has to be significantly higher than the energy of the x-ray peak to be measured. Energy of incoming electrons also determines how deep signal can originate. Beam current also has to be increased from imaging level to get enough signal for x-ray analysis. As the detector

can only process single photon at a time, too high current leads to coincidence peaks filling the spectrum. [50]

X-ray peaks below 4 keV have only small energy differences, therefore having a high risk of misidentification. As photon absorption is strong in range of about 1 keV above the critical ionization energy of other elements present, it can mask a signal from elements with characteristics peaks within this range. Especially problematic this would be in samples that consist of elements with low energy peaks only or when using low beam energies. [50]

2.2.3 XPS

In XPS, x-rays are used to ionize atoms by kicking out an electron from core levels. Binding energy (BE) of the electron is then determined from its kinetic energy which $E_k^e = hv - BE - WF$, where WF is the work function defined as the distance of the Fermi-level from the vacuum energy level. Element can be identified by comparing measured BE value to known values. Shifts in BE can allow determination of what atoms the ionized atom is bonded with as it might hold its electrons little tighter or looser depending on its environment. [51]

X-rays are generated by bombarding the x-ray anode with electrons that ionize atoms in it by removing electrons from core levels (Figure 8), which then relaxes to a lower energy configuration when an electron from higher energy level drops to the vacant position and radiates photon. The x-ray energy depends on the anode material. Generated x-rays are then send to monochromator and focused on small spot on the sample surface. Measurements of solids are done in ultra high vacuum. [51]

XPS can only give information about the sample surface, about 10 nm layer. If information about even shallower depths is wanted the sample can be tilted so x-rays hit the surface at smaller angle and distance electron has to travel to leave

the sample increases relative to depth. Second approach to depth profiling is to use sputtering remove material layer by layer while doing analysis between sputtering rounds. [51]

2.2.4 XRD

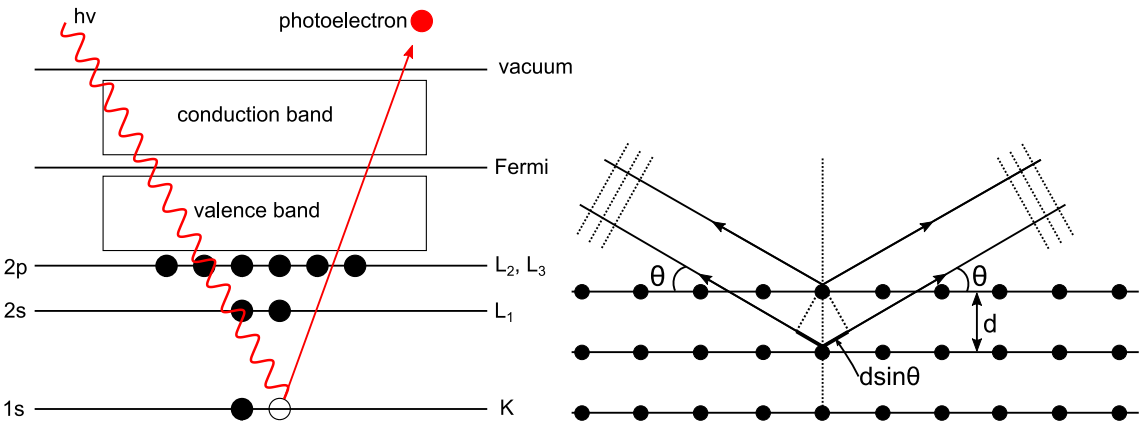

Figure 8. On the left principle of photoelectron release from solid in XPS is shown. On the right a diagram depicting Bragg diffraction.

In XRD, a diffraction pattern is used to determine the crystal structure of the sample under investigation. The pattern is produced when x-rays hitting the crystal are reflected from different lattice planes in the sample interfere with each other as they have travelled different distances and are therefore in different phases. Used wavelengths are comparable to interatomic distances. [52–54]

The diffraction condition is known as Bragg's law $n\lambda = 2dsin\theta$, where d is the interplanar spacing, θ the angle between incoming beam and the sample surface, λ the X-ray wavelength, and n any integer (Figure 8). [52–54]

Only in monocrystalline material sharp intense peaks are detected. Amorphous materials have no diffraction peaks, while in polycrystalline materials peaks are broader and less intense than in monocrystalline material. [52–54]

The diffraction pattern consists of multiple peaks, which correspond with specific lattice planes. Distances are measured as an angle between surface and incoming

x-rays. The strength of the diffraction peaks depends on the electron density of the crystal plane, which depends on atomic number and density. [52–54]

The diffraction peaks widen slightly due to nonidealities related to the x-ray beam, such as non-zero bandwidth and beam size, and crystal. The peak locations are also shifted by lattice strain. [52–54]

The experimental results only give the intensities of scattered x-rays, so to determine crystal structure one has to fit potential structure to the diffraction pattern. Then calculated pattern is compared with measured pattern and fit modified before repeating the process until fitted structure matches the experimental result. [52–54]

Diffraction from nanomaterials is different from bulk matter mainly due to multiple surfaces contributing to the pattern simultaneously and other effects related to finite size. These effects are visible unless crystal is much larger than x-ray spot size, typical spot sizes on laboratory equipment are around 100 µm. [52–54]

Nanomaterials are often investigated with either powder diffraction, small-angle diffraction or grazing incidence diffraction methods. [52–54]

2.2.5 AFM

AFM is one scanning probe microscopy method and is typically used to investigate surface topography. In AFM the sample surface is investigated with a very sharp probe tip on a cantilever, whose size can be even in nanometre range. The height resolution can be even a fraction of nanometre and lateral resolution about nanometre depending on tip size. If the feature on the surface is smaller than tip size, tip shape determines measured profile (Figure 9). To achieve correct result the tip has to be much sharper than the feature to be measured. [55]

Interactions between the sample surface and probe tip are governed by van der Waals forces, whose strength and direction depend on the tip-surface-distance (r). At close range repulsive potential of type B/r^{12} affects the tip and when range

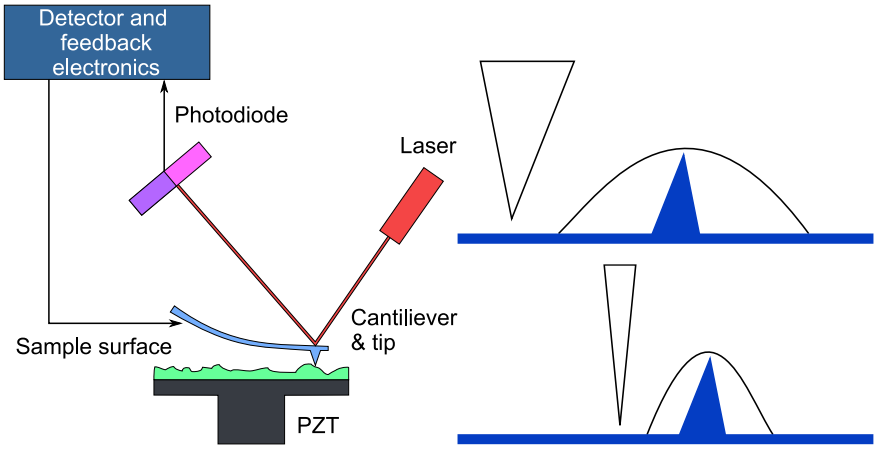

Figure 9. On the left a block diagram of AFM system modified from a Public Domain image in Wikipedia. On the right a diagram depicting effects of tip size to measured topography.

increases potential becomes attractive $-A/r^6$, A and B are constants. [55]

AFM can be operated in contact, tapping and non-contact modes depending on sample composition and desired investigative objective. In contact mode the probe tip touches the surface continuously during the measurement and follows the surface profile continuously due to repulsive interactions. This provides the highest possible resolution and risks surface damage. [55]

The tapping mode is a compromise between contact and non-contact modes, where the tip lightly touches the sample surface. The vibrational amplitude varies according to surface topography during the scan with repulsive interactions still governing but much closer to potential minima than in contact mode. It provides almost as good resolution than in the contact mode. [55]

In non-contact mode tip to surface distance is at least multiple nanometres and interaction type is attractive, which minimizes the risk of damaging the sample but decreases resolution significantly. [55]

The cantilever position is measured by reflecting laser from the end of the cantilever to a position sensitive detector consisting of two closely spaced photodiodes, whose output is sent to differential amplifier (Figure 9). The deflection of

the cantilever is proportional to amplifier output as the angular displacement of the cantilever leads to one photodiode collecting more light than other. Maximum measurable height difference depends on the maximum deflection of the cantilever and usually around 10 µm. [55]

2.2.6 Optical

In photoluminecence measurements of semiconductors, the sample is excited with photons that have much higher energy than bandgap exciting electrons from the valence band to the conduction band. The resulting holes and electrons relax then to bandgap minimum before recombining radiatively by emitting photon. Typically, a continuous-wave laser is used as excitation source. [56]

The wavelength of emitted light gives information about electronic and optical properties of the sample. Excitation is usually done with UV wavelengths and emission is in visible light range. The experimental system is build in a way that prevents incident light from reaching the detector with either filter or diffraction gratings. In chemistry, this method is known as fluorescence spectroscopy. [56]

In nanomaterials at least one dimension is often small enough that quantum confinement comes to picture leading to density of states totally different from bulk material. Photoluminescence spectrum of quantum wires is much more intense than bulk material and has multiple sharp peaks due to transitions between discrete energy levels arising from the quantum confinement. The intensity increase is due to the higher density of states. [56]

Reflectance measurements are done with optical spectrometer where the sample illuminated with monochromated light from a broadband lightsource. The wavelength is then changed with constant step size from UV to near infrared while the amount light reflected from the sample is measured.

2.3 Analysis methods

SEM images and AFM data were analysed with open-source software packages Fiji and Gwyddion respectively [57]. Size distributions, surface densities, and the total volume of nanocrystals was acquired from SEM images, while AFM data was used to extract information about surface roughness. XRD data was collected and analyzed with HighScore plus software package [58].

As the Fiji software includes machine learning plugin Trainable Weka Segmentation, it was used to extract previously mentioned information from SEM images. The first task is choosing good settings for features to be used for training and classifier type. To ease the process slightly a macro was used to run preprocessing and particle analysis steps for each image, while classifier was run manually. [59]

The used classifier type was MultiLayerPerceptron with default settings. For training selected image was cropped so that both dimensions were below thousand pixels, then for ETD images FindEdges function was used for preprocessing before segmentation. The trained classifier was then used for selected ETD images with the bottom infobar removed after the preprocessing step. Some images had to be further cropped to exclude contaminant particles, edges or at boundaries other side. Training the classifier required marking different areas being member class one or two.

After segmentation AutoThreshold function with Shanbang method was applied to the segmented image with "BlackBackground" option set false. The next step was setting scale (pixels/µm) and running AnalyzeParticles function to determine percentage of total surface area covered by nanocrystals.

T1 images were segmented with Weka classifier trained for T1 images after applying enhance local contrast function to them and directly with Robust automatic segmentation. Segmentation for T1 was also run after background subtraction with sliding parabola option. This was followed by total crystal area determination as

with ETD images.

The first step in analysis of the AFM data is levelling to ensure that surfaces that should be vertical are vertical. Then imaging artefacts and outliers can be removed and roughness analysis run. Gwyddion can calculate roughness for area sizes starting from line and going up to 128 pixels wide area. This gives two datasets per scanned site so final value will be calculated as RMS value from these two.

For levelling "Facet Level" function was used and then a profile line drawn to the image with Profile tool. If the scanned area has particle or similar large peak they can be removed with "Mask of Outliers" tool followed by "Remove Data Under Mask" command. The roughness analysis is done with Roughness tool that calculates roughness and waviness, where the latter defines overall shape of the surface texture as low-frequency components. Gwyddion user guide gives following expression for RMS roughness $\sqrt{1/N \sum_{j=1}^{N} r_j^2}$, where $r_j = z_j - \overline{z}$ and z_j the jth value in height (z) vector with $\overline{z}$ being average height.

Binding energies of XPS peaks were picked manually from numerical data as the datasets were small. Compounds matching these peaks were identified from NIST X-ray Photoelectron Spectroscopy Database [60]. Potential choices were limited by knowledge what elements can be present in the sample.

3 Experiments

This chapter provides a short description of used equipment and other experimental details.

3.1 Equipment

Samples were analysed with following equipment: SEM, XPS, XRD, AFM, optical spectrometer, and fluorescence.

Thermo Scientitific Apreo S SEM used in this work has beam energies in 0,2–30 keV range and currents from 1 pA to 400 nA. It was equipped with eight different detectors, but in this this work only BSE detector, ETD, and EDS were used. The column has two additional SE detectors with energy filtering. All measurements were done in high vacuum, with chamber pressures below 4×10^{-5} mbar. A navigation camera eases navigation on the sample surface.

The attached EDS was Oxford Instruments Ultim Max 100, which has Peltier cooled 100 mm^2 sensor capable of detecting elements from Be to Cf. The AZtec software provides elemental mapping capabilities.

The AFM measurements were done with Bruker Innova Nano AFM that can operate in contact and tapping modes. The lack of an air table made the instrument more sensitive to external vibrations reducing resolution. Samples were attached to a piece of carbon tape on a steel disk that was held on stage with a magnet. This procedure caused sample contamination and the sample position was not horizontal.

Thermo Scientific Nexsa XPS was used to study chemical and elemental composition. In addition, of XPS, the device is also capable of ion scattering spectroscopy, ultraviolet photoelectron spectroscopy and reflection electron energy loss spectroscopy. For depth profiling and surface cleaning ion source, which provides either individual ions or clusters, is installed. A tilt module enables Angle Resolved XPS to investigate the sample even closer to surface than 5–10 nm range in reg-

ular XPS. Samples are moved to the analysis chamber held in ultra high vacuum though a loadlock with a motorized stage. The X-ray source is a monochromated Al Kα-source.

Crystal structures were investigated with Pananalytical Empyrean XRD. This instrument has software controlled 5-axis stage, also Anton Paar TTK450 and Anton Paar HTK16N low- and high temperature chambers are available. Two detectors are available a gas-filled proportional counter (point detector) and PIXcel3D solid state area detector, latter was used in this work. The installed x-ray source is Cu Kα-source with acceleration voltage up to 45 kV.

Sputtering and heat treatment were done with an old custom build ultra high vacuum multi chamber system consisting of loadlock, preparation and analysis chambers. The system was equipped with a scanning tunneling microscope, XPS, and low energy electron diffraction capabilities installed for analysis. Ar^+ ion sputtering was also possible.

The sample had to be manually transferred to correct position in the second chamber from the loadlock with manipulator arms requiring switching arms with stage in the first chamber. The positioning screws had measurement scales to enable positioning. Resistive heating elements integrated into the stage were used for the heat treatment.

3.2 Experimental arrangements

Chemical processing was done in fumehood. Used chemicals were VLSI grade. Mass percentages of HCl, H_2O_2 and NH_3 solutions were 37 %, 30 % and 28–30 % respectively. Standard preparation protocol for samples before synthesis involved 180 s ultrasound cleaning in IPA to remove organic residues and particles from the surface, for most of the samples native oxide was removed with 180 s etch 3:1 IPA/HCl solution followed with 60 s IPA bath of which 30 s was in ultrasound.

In total 24 samples were processed during the experiments and one extra unprocessed sample (s83) was used as reference for optical measurements and XRD. Most of the samples were pieces of n-type GaAs (100) wafer with size of 5 mmx11 mm, three times the sample was halved and pre-synthesis processing was done to both pieces while synthesis was only done with the second piece. Three last samples were pieces of p-type GaAs (100) wafer (Zn doped) with similar size than original samples. All pieces come from single side polished prime grade wafers.

For synthesis a 100 mL container was filled with type 1 ultrapure water (21 MΩ cm) and then heated with a hot plate to 80 °C. The temperature on the surface of the hot plate had about 20 °C difference between the hottest and coldest spot. During heating water and plate surface temperature were checked regularly with an infrared thermometer. During cooling/heating cycle water temperature remained within ±5 °C of the target.

As water level in the synthesis decreased about 35 mL/h, about 40 mL pre-heated water was added to the synthesis container about 1,5 h from the start of synthesis. Total synthesis time was 150 min, all times were measured with a stopwatch. All other parts of the process were done in about 25 °C.

Bubbles formed at tips of the tweezers and moved upwards along the tweezer. Size of bubbles increased at tweezer-sample interface. Bubbling was especially strong when water level was below 30 mL.

The chemical harvesting test was done in solution with 13:6 ratio of hydrogen peroxide and ammonia solutions, the etching time was 100 s followed by two dips into water in two containers for 40 s in time.

For chemical roughening tests the hydrogen peroxide to ammonia ratio was 20:1, pH of this solution measured with indicator paper was over ten, followed by 30 s dip into water. Etching times for chemical roughening were 120 s and 20 s. Before roughening, 180 s IPA US cleaning was done.

The chemically roughened samples were measured with AFM in contact mode to determine their roughness. Due to time constraints measurements were done from multiple sites for only one sample. Scan ranges of 5 µm, 10 µm and 50 µm were used for every site.

Ar^+ sputtering was done with 1,0 kV energy and 10 mA current. The beam controls were set to move the beam over 10 mmx10 mm area. The total sputtering time was 660 s with the sample moved on time period 330–350 s 7,0 mm while the beam was kept on. One sample was sputtered at 350 °C while the other two were kept at about 20 °C. The gas flow for sputtering was set a certain level by monitoring chamber pressure as a leak valve in the gas line was opened. The chamber pressure during sputtering was about $8{,}2 \times 10^{-8}$ mbar.

For heat treatment and sputtering at elevated temperature, the temperature was increased stepwise to prevent outgassing increasing too much and to reduce thermal stresses affecting the sample. The temperature was controlled by changing voltage and current to the heating elements. One synthesized sample with GaOOH nanocrystals was heat treated at 450 °C for four hours to transform it into an oxide.

In XRD measurements the sample was attached to about 2 cm high amorphous stub with adhesive, which was then attached to the metallic sample holder. This reduces the interference of the metallic holder to the measurement. The x-ray generator was run at 45 kV and 40 mA.

Before actual measurement a calibration was done to ensure that x-ray source and detector are aligned and x-rays hit sample surface specific spot. In the measurement only x-ray source and detector moved relative to the sample, which was kept still. This measurement type is known as 2θ-ω-measurement, where θ is the angle of X-ray relative to the sample surface. Theta changed from 5° to 90° with constant step size.

Seeds for seeding experiments were collected by doing a synthesis as per standard

protocol and then scraping the sample surface with a blade in IPA or water. In the first seeding experiments, seeds were in IPA, but later the seed solution was dried and solvent changed to water.

Arsenic concentration was measured semiquantitatively with Supelco MQuant Arsenic Test. The test is based on reactions of AsH_3 on the reaction zone of the test strip containing $HgBr_2$ changing colour of the zone, which is then compared reference. Generation of AsH_3 happens when zinc powder, a solid acid and to eliminate interfering sulphide ions an oxidizing agent are added to water containing arsenic(III) and arsenic(V). These reagents are added one at time and mixed after each addition. After the third reagent is mixed to the water the test strip is inserted and left inside the reaction bottle for 20 min, during this time the solution is carefully swirled for two or three times.

The amount of arsenic in the synthesis water after synthesis is calculated by multiplying the measured arsenic concentration with the dilution factor and the amount of water left after synthesis.

When estimating the amount arsenic released during synthesis, it is assumed that all surfaces of the sample react with equal rate and the sample thickness is 500 µm, allowing total surface area of the sample used. The thickness (d) of reactive layer is calculated from the amount arsenic in the synthesis water after synthesis by converting the mass of arsenic to moles, which then converted to mass of GaAs and to volume based on density. Following formulas are used to calculate the thickness $d = V/Ad$, $V = m/\rho$, $n = m/M$, where V is the volume, A the area, m the mass, ρ the density, n the amount of substance and M the molar mass. The final equation is $m(As)/M(As) * M(GaAs)/\rho(GaAs)/A(GaAs)$.

4 Results

4.1 Results

At first properties of samples, which have gone through only the previously mentioned cleaning protocol, after synthesis are discussed as they provide a baseline to which samples with additional treatments are compared to. Here surface density refers to the amount of surface covered by nanocrystals per unit area. Coloured markings are used in some images to indicate features of interest.

4.1.1 Baseline

Synthesized crystals can be up to 1,1 µm wide, with typical width range of the nanocrystals 700–800 nm (Figure 10). However, the smallest found nanocrystals are only about 20 nm wide and while widths below 100 nm are rare, significant amount of the nanocrystals have widths in the 200–500 nm range.

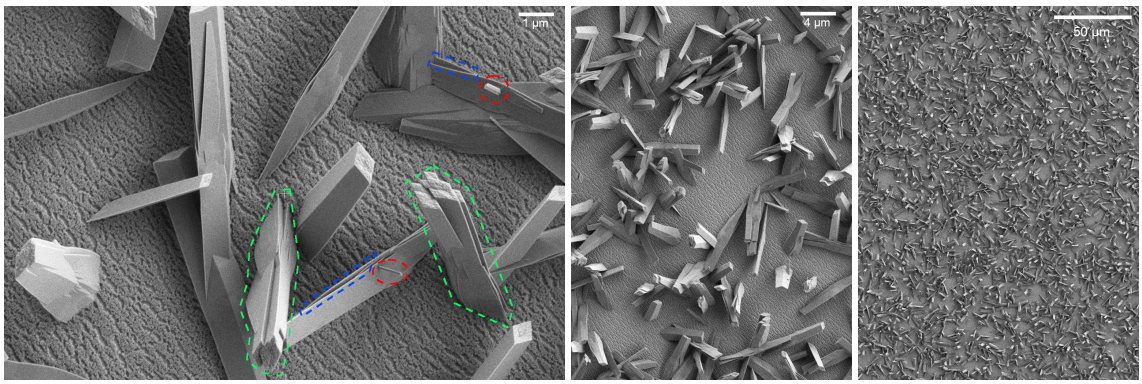

Figure 10. SEM image nanocrystals produced with standard process. On the left small crystals sticking out from the side of larger crystal (red line) are seen as well a crystal consisting of multiple individual nanocrystals partially fused together (green line) and thin crystal slabs (blue line). On the middle groupings and large open spaces between them in addition to some isolated nanocrystals are visible. The low magnification image on the right enables visual comparison of surface density with later samples.

The crossection of the nanocrystals is not rectangular, as its angles are about 60° and 120°. The aspect ratio, length/width, is below ten and for some nanocrystals

it can be about three. Many of nanocrystals thicken towards their base at substrate/nanocrystal interface, though the crossection of some nanocrystals appears to stay constant for their whole length.

Crystals exist in groupings, where the nanocrystals sometimes even cross each other, though some nanocrystals do not belong to these groupings and are isolated. Empty spaces in the range of 5–10 µm exist between groupings. Figure 10 demonstrates these features.

Smaller nanocrystals can be found attached to the sides of the larger nanocrystals with varying sizes. The largest attached crystals were up to half or third of the host nanocrystal, though many are much smaller. Nanocrystals grow at varying angles relatively to the substrate surface, the angle distribution covers practically the whole range from zero to ninety degrees. Many nanocrystals grow at relatively small angles. The orientation of the projections of the nanocrystals to the substrate surface are random.

Thin slabs/sheets are also visible in the SEM images with thicknesses down to 20–30 nm and typically about 60 nm. Some nanocrystals appear to consist of multiple nanocrystals partially fused together. See Figure 10.

4.1.2 Scraped and reprocessed

Scraping a processed sample and reprocessing it results in areas of small nanocrystals with high surface density. Individual nanocrystals can also fuse together covering the whole surface on some areas, on the other hand areas with no nanocrystals or only a few small nanocrystals, typically below 200 nm, also exist. One sample (s79) was scraped from both sides and after reprocessing surface of s79 was almost totally covered, the coverage consisted of a layer of small crystals on top of large ones (Figure 11).

In some regions parallel areas with no nanocrystals exists with nanocrystal con-

taining areas in between, the direction of longer side of these areas is consistent with the scraping direction. The boundary between scraped and non-scraped areas is relatively clear with about 15 µm wide transition region where small nanocrystals with high surface density exist based on SEM images. Most of this high density growth is in about 8 µm wide area (Figure 11).

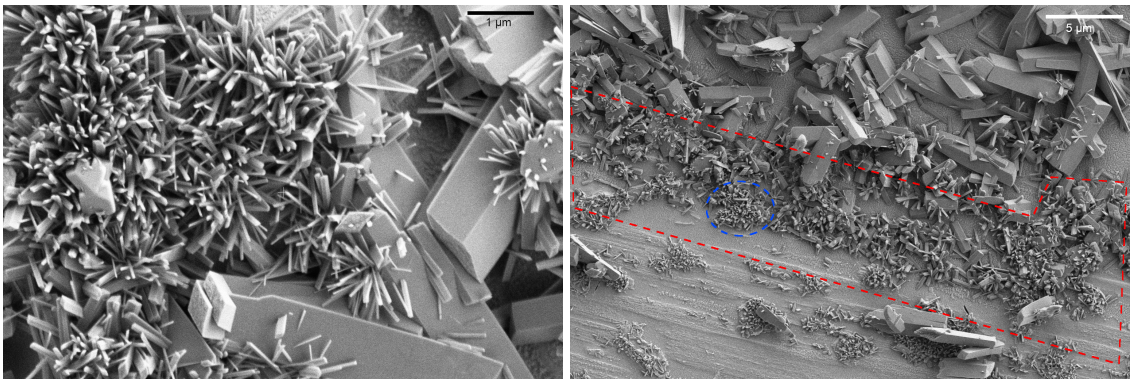

Figure 11. SEM images of nanocrystals in scraped and reprocessed samples, showing region with thin nanocrystals on top of large nanocrystals on the left and the transition region (red line) between scraped and non-scraped areas with small crystals (blue line) at boundary on the right.

The substrate surface has cracks even 100 nm wide and in areas with no nanocrystals cracking of the native oxide from surface is seen in SEM images leaving multiple microns sized spots where GaAs surface is visible (Figure 12).

Scraping removes most of nanocrystals from scraped areas while leaving behind some pieces, of which some move over the boundary to non-scraped area. Pieces of cracked nanocrystals, typically in the width range of 700–800 nm and even up to one micron, acted as hosts for up to 100 nm wide nanocrystals. The smallest nanocrystals on the host crystals were in 20–30 nm width range and could be classified as nanowires. See Figure 11.

In some areas broken pieces of large nanocrystals are mixed with new growth of small nanocrystals and in some other areas dense fields of small nanocrystals were detected. Often crystal formations best described as nanoflowers existed on top of large crystals. Diameters of these flowers varied from about 1 µm to about 2,5 µm

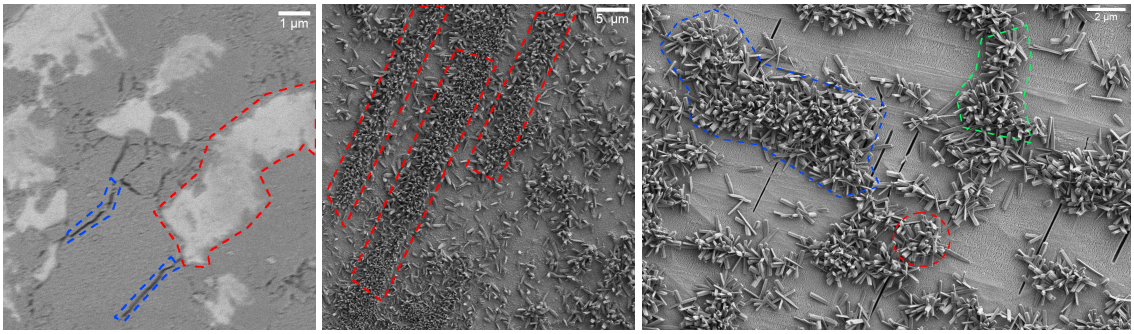

Figure 12. On the left partially cracked oxide layer with GaAs surface visible (red line) along with cracks (blue line), the second image from the left shows parallel high density areas (red line) of nanocrystals, while the image on the right has single nanoflowers (red line) and their formations (green and blue lines).

and usually they form groupings that can have dimensions even over ten microns. Also, non-circular flower like regions were detected that can be up to 4 µm wide and 9 µm long. See Figure 12.

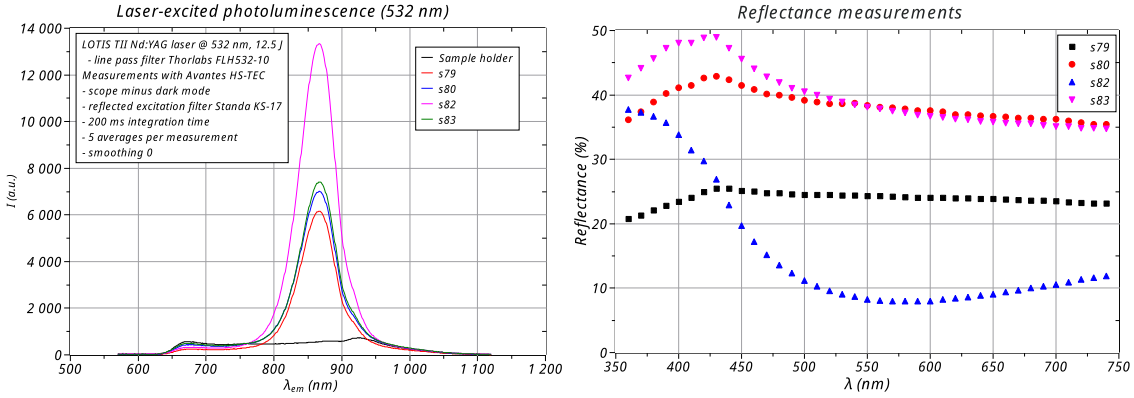

Figure 13. Photoluminescence and reflectence of s79 (reprocessed), s80 (seeded), s82 (chem. roughening 120 s+synthesis) and s83 (reference, GaAs piece). In the reflectance measurement notable features are low reflectance values of s82 for longer wavelengths and then rapid increase when moving towards shorter wavelengths, similarity of s80 and s83 for λ>500 nm and s79 having significantly lower values than s83. Note how the photoluminescence peak of all samples is at the same position (865 nm) and significant differences in the peak heights, especially for s82.

Figure 13 shows that the photoluminescence peak height of s79 is about twenty percent lower than s83 (reference), the reflectance curve for s79 is raised steadily with total increase about 10 % down to 425 nm and then dropped about 20 % from the peak value over next 75 nm. Rate of increase for s79 towards lower wavelengths

is less half of the corresponding value for s83. The peak reflectance for s79 (26 %) is about half that of s83 (50 %) with both being at the same wavelength (425 nm).

4.1.3 Roughening

Scraping the sample (s67) before synthesis results in areas with no crystals corresponding to scraped areas. Small spherical particles up to 1,1 µm, but typically in 700–800 nm range were detected in scraped areas and in their edges. EDS results show that these particles do not contain gallium, while having oxygen and slightly increased arsenic concentration (Figure 14).

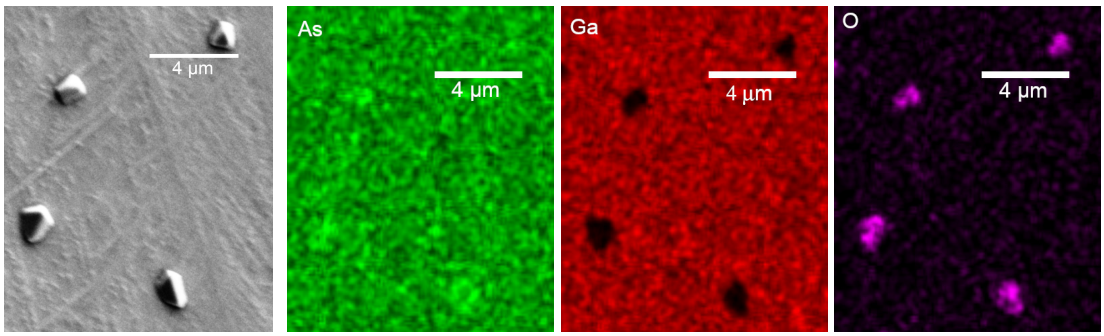

Figure 14. SEM image and EDS elemental maps showing presence of potential arsenic oxide nanoparticles on GaAs surface in s67. Map colours: green=As, red=Ga and violet=O.

Chemically roughened samples (s69-74, s82) have after synthesis cracking native oxide surface, which has holes where bare GaAs surface is visible (Figure 16). The synthesis step leads to appearance of small amount of particles, of which some are gallium oxide based on EDS data. Some arsenic oxide nanoparticles were detected by EDS on sample (s71) that was chemically roughened for 20 s before the synthesis step (Figure 15).

XPS analysis of chemically roughened samples indicates presence of arsenic and gallium oxides, As_2O_3, Ga_2O_3, $GaAsO_x$ and possibly As_2O_5, on surface before and after synthesis step. On samples (s70, s73) kept 120 s in the roughening solution without the subsequent synthesis step in As 3d scan a strong peak was detected at

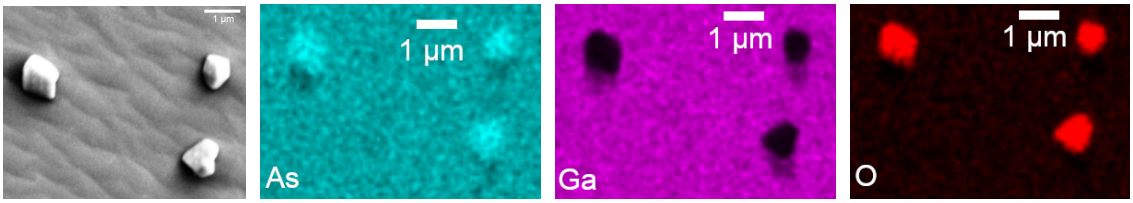

Figure 15. SEM image and EDS elemental maps showing presence of arsenic oxide nanoparticles on GaAs surface in s71. Map colours: light blue=As,violet=Ga and red=O.

41,5 eV corresponding to GaAs/Ga in addition of arsenic oxide peak at 45,0 eV and peak height was over three times higher than the oxide peak. In the Ga 3d scan for s73 the peak at 19,8 eV corresponds to Ga, GaAs or GaO_x. The Ga 3d scan of s73 has a small kink at slightly lower binding energy than the maxima of s74, in the As 3d scan around 45 eV s73 has slightly lower intensity and different peak shape than s74 while peak maxima has shifted to higher binding energy. Bulk Ga and As are not seen after the synthesis step. See Figure 16.

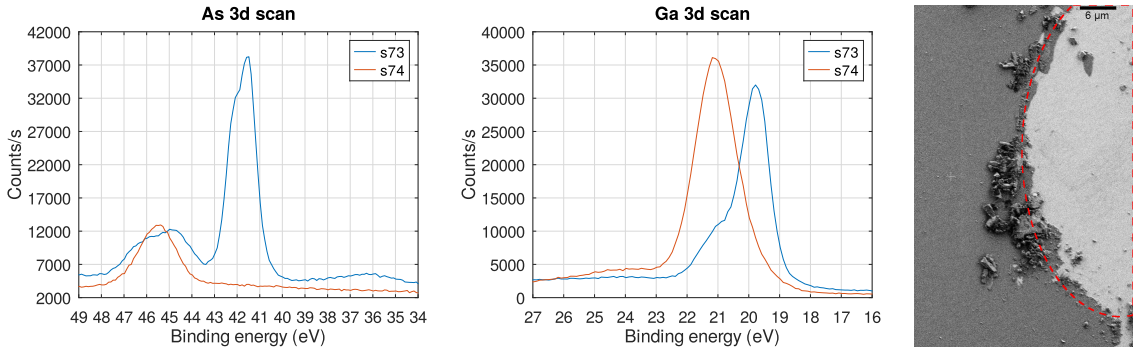

Figure 16. As and Ga 3d scans of chemically roughened s73 and s74, equivalent to s70 and s69. Note the differences between XPS results of s73 and s74 caused by synthesis step for s74: different peak shapes, shifts to higher binding energies for the peaks at 45,0 eV and 19,8 eV, intensity changes and disappearance of the large peak at 41,5 eV in the As 3d scan. On the right SEM image from s69 (equiv. s74, s82), shows dark areas with oxide layer and lighter areas with substrate visible where the oxide layer has broken (red line).

The photoluminescence peak of s82 is almost double that of s83 and reflectance of s82 behaves completely differently than s83 as it has minima around 580 nm and no maxima. The reflectance minima for s82 is about 20 % of reflectance of s83 at

the same wavelength. Then reflectance starts increase rapidly until about 425 nm when the rate of increase starts to decrease with probable maxima just outside measurement range. Figure 13 demonstrates these matters.

Both SEM images and AFM data (Figure 17) indicate surface waviness with amplitudes even over 20 nm. RMS roughness varies significantly over sample surface depending on what spot AFM data was collected and position, direction and size of profile window for which these parameters were calculated.

The values of roughness and waviness are given in Table IV for all four samples measured with AFM. Roughness of GaAs wafer surface with native oxide is about 0,2 nm, so measured the chemically roughened surfaces are at leat four or fives times rougher than wafer surface and one measurement is about seventeen times larger. The waviness of synthesized samples is higher than in non-synthesized samples. The AFM results should be considered indicative only due to measurement uncertainties present.

Table IV. Roughness and waviness, see Chapter 2.3 and Gwyddion user guide, of chemically roughened samples before and after synthesis step. RMS values are used. The first two samples (s69,s70) were etched for 120 s and the latter two (s71,s72) for 20 s. No synthesis step for s70, s72. The column s72 t contains RMS value of corresponding values for all three measured regions in s72. Note that scanned areas for s72 r3 and 10 µm area for r1 had particles present, causing differences between the measurements. The markings in braces tell the size of the scanned area (square).

	s69	s70	s71	s72 r1	s72 r2	s72 r3	s72 t
roughness (5 µm)	1,0 nm	0,82 nm	3,4 nm	0,92 nm	0,74 nm	1,6 nm	1,1 nm
waviness (5 µm)	8,2 nm	4,3 nm	24 nm	15 nm	2,5 nm	7,6 nm	9,6 nm
roughness (10 µm)	1,0 nm	0,82 nm	2,1 nm	2,4 nm	0,36 nm	2,8 nm	2,1 nm
waviness (10 µm)	9,8 nm	4,3 nm	7,2 nm	5,7 nm	6,9 nm	8,9 nm	7,3 nm

Sample sputtered at room temperature (s85) has small holes on substrate surface. Nanocrystals on sputtered areas are about 10–20 % smaller, often width is 600–

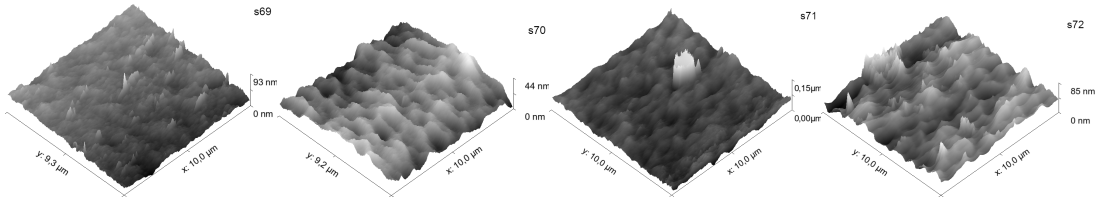

Figure 17. AFM images of the two pairs of chemically roughened samples. From left to right s69, s70, s71 and s72. For s71 nanoparticle in the scanned area was excluded and the white area contains whatever is left after exclusion. Note that the height range is different in each image.

700 nm, (Figure 19) and have lower surface density than in non-sputtered areas where nanocrystals have the same width distribution than seen in the baseline samples. If sample was heated during sputtering (s86) the surface density in sputtered areas is slightly higher than in non-sputtered areas but lower than in the sample sputtered at room temperature. Figure 18 illustrates these matters.

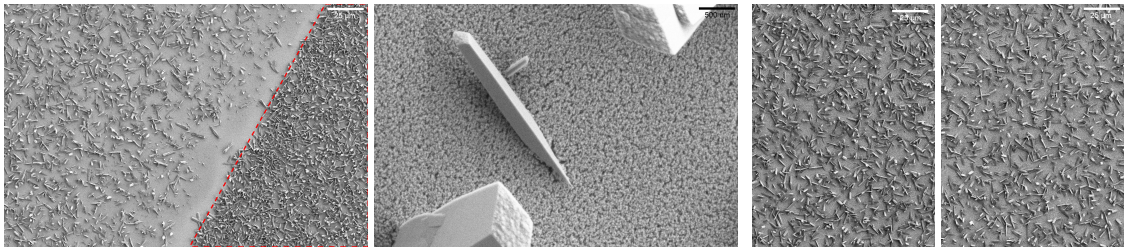

Figure 18. The leftmost SEM image is from boundary between sputtered (left) and non-sputtered (right) areas of s85 showing significantly decreased surface density of nanocrystals due to sputtering at room temperature, note the at least few microns wide area without nanocrystals at interface. The boundary trends in the image towards left when moving towards bottom of the image, marked with red line that also surrounds the whole non-sputtered area. On the second image from left surface of s85 is shown with high magnification and surface effects of sputtering, such as small holes, can be seen. The two rightmost images are from sample that was heated during sputtering (s86), with the second image from right shows sputtered area and the rightmost one non-sputtered area.

Based on segmentation and subsequent analysis sputtering could reduce surface density between one third and half. In sample heated during sputtering non-sputtered areas have about 10–20 % lower surface density than sputtered areas. Results of segmentation of T1 detector SEM images after background subtraction are given in the Table V.

Table V. Area of surface covered by nanocrystals based on segmentation with Weka. T1 images were used. Note the inconsistencies with larger imaging area sizes. Values in percent of total area, if multiple images exist for the same sample from the same region mean value is given. Likely error level at least 10 %. The first two results (s90, s68) give baseline, marking a after sample code indicates non-sputtered area and b sputtered area, s85 was sputtered at room temperature and s86 at 350 °C. s84 had seeds introduced to synthesis water.

Imaging area (µmxµm)	s90	s68	s85a	s85b	s86a	s86b	s84
63,5x42,3	51	48	51	34			
84,7x56,5				44	32	39	34
106x70,7				58			40
127x84,7			63	32			38
195x130		50		56	40	44	
254x169		54		50	43	49	
363x242	67			63			50

An example of segmented image is given in the Figure 19 showing quite good result, while illustrating areas where substrate is misclassified as nanocrystal in the middle of group of nanocrystals and widening of areas classified as nanocrystal. Segmentation data indicates sputtering induced reduction in surface density of nanocrystals between 30–50 %, with further decrease due to heating during sputtering noted being up to 10–20 %. Non-sputtered areas on sample heated during sputtering show 10–20 % lower surface density compared to sputtered areas (Figure 18) in the segmentation results.

4.1.4 Seeding

Seeding results in areas of small nanocrystals with high surface density, but most of the sample does not show any change. Flower like growth over larger crystals are visible in the SEM images, consisting of individual nanocrystals pointing outwards from the centre to every direction (Figure 20).

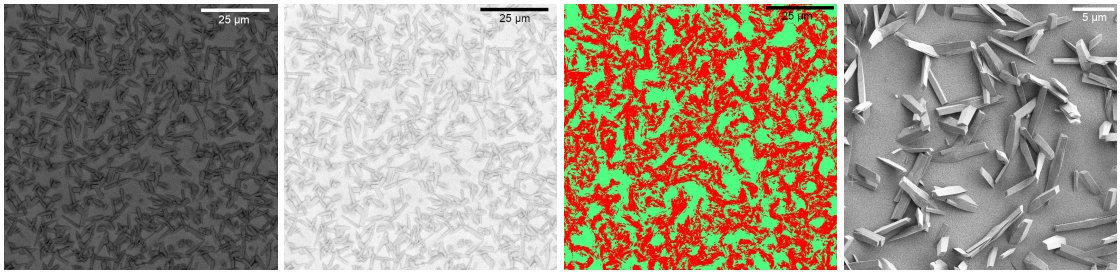

Figure 19. From left to right original T1 detector image from sputtered area of s85, background substracted image and segmented image, where red is classified as nanocrystal and green as substrate. The fourth image on the right shows nanocrystals in the sputtered area of s85.

The sample seeded with pipette from the lowest concentration seed solution used in these experiments has small particles and crystal pieces over the normal crystals. Significantly increased local surface coverage was detected with no small crystals, while most of the surface shows no changes compared to baseline samples (Chapter 4.1.1). Spots of higher surface density along with flower like spots of small crystals on top of larger crystals can be found from SEM images (Figure 20).

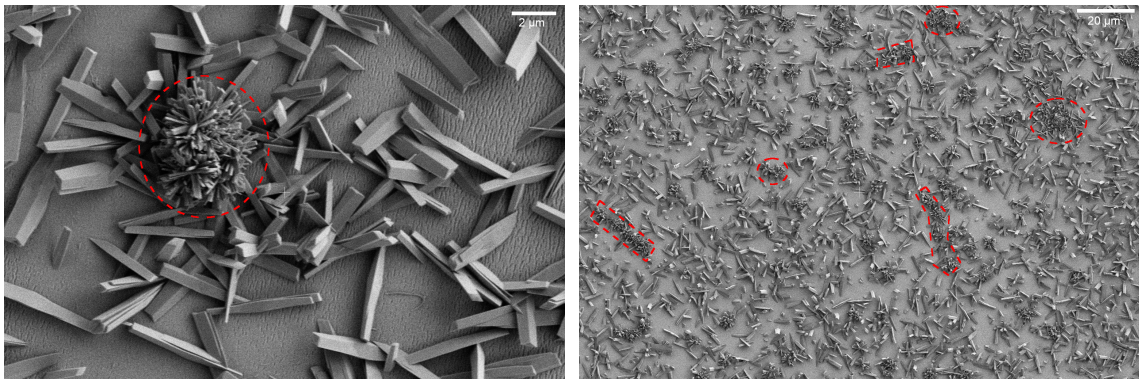

Figure 20. SEM images two seeded samples (s78, s80) showing close-up of one flower like region (red line) and overview of larger area with high surface density regions (red line) at multiple spots among with normal nanocrystals elsewhere. For s80 on the right side image higher concentration seed solution was used.

The second seeding attempt (s80) provided similar results to the first but higher amount of high surface density areas. Higher concentration seed solution was used in the second attempt compared to the first. In some regions the substrate surface looked slightly porous and nanocrystals were thinner than elsewhere (Figure 21).

Photoluminescence and reflectance results from Figure 13 show that the value of the photoluminescence peak for s80 is only about 5 % lower than for s83, while reflectance has at most a few percent difference to s83 until about 500 nm. At lower wavelengths reflectance of s80 does not increase as fast as s83 with maxima (43 %) being about 10 % lower than in s83 (48 %).

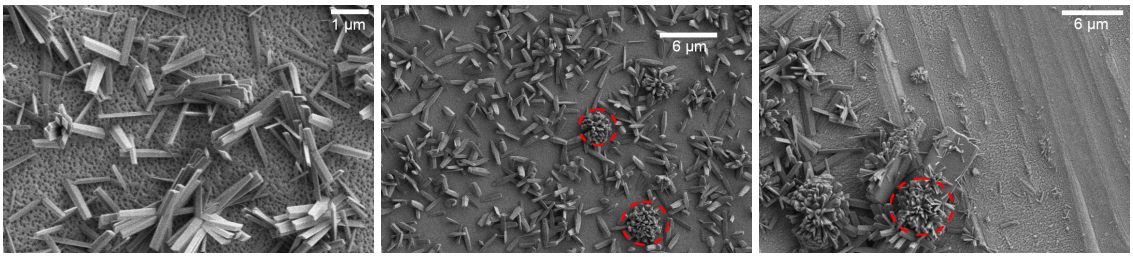

Figure 21. SEM images from two seeded samples (s80, s81) showing porous like area in s80 on the left. The middle image shows flower like spots among normal nanocrystals and on the right a close-up of growths on top of large crystal piece is shown among with scratched area with only some very small growths. The flower like growths are marked with red line.

The sample (s81) dragged along the bottom of the seed container and left there overnight has again spots with flower like growth. Now, the sample has similar large areas with only some small particles seen in the scraped samples. SEM images show also some flower like growths forming very dense ellipsoids with the ends of the crystals forming almost continuous surface. In many spots growths on top of crystals were detected, while most of the surface matched with the baseline. The amount of dense spots was also higher than in previous seeding attempts. See Figure 21.

Introducing seeds to the synthesis water (s84) results in relatively uniform surface density, which is higher than in the baseline samples but smaller than the dense spots in other seeded samples. The resulting nanocrystals are smaller than in the baseline samples as typical nanocrystal widths are 400–500 nm and some are up to 600 nm. These are about 20–30 % smaller than nanocrystals in the baseline samples. Figure 22 illustrates these matters.

At some points cracks exist at nanocrystal/substrate interface. In the circular area terminating to the shorter edge of the sample oddly shaped nanocrystal with low surface density were found, along with some small bumps on substrate surface. Segmentation based surface density analysis gives very low surface density, comparable to sputtered samples.

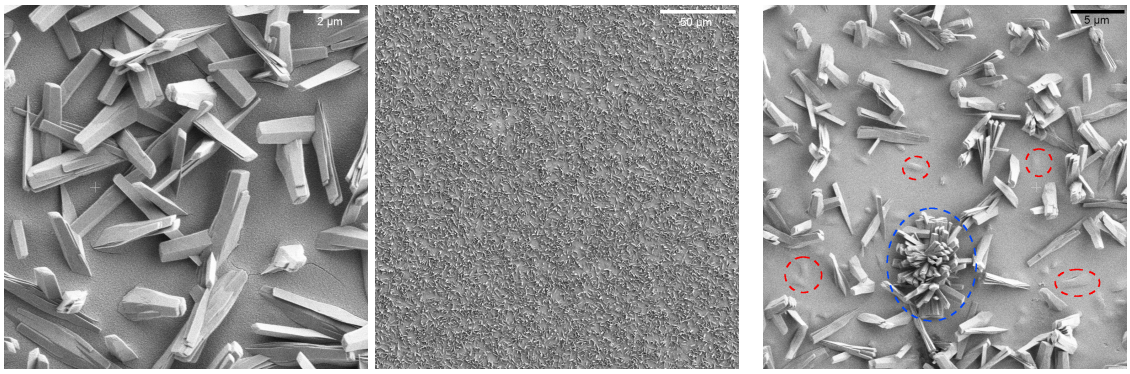

Figure 22. The two first SEM images from left are from sample (s84) with seeds introduced to synthesis water showing high surface density in image from larger area, the close-up shows the formed nanocrystals. On the right sputtered sample (s87) that was overnight in water containing seeds and small bumps clearly visible on surface along with single nanoflower. Bumps are surrounded with red line and nanoflower with blue line.

Seeding sputtered sample that was left to water containing seeds almost for a day showed similar results as to other seeding experiments, but on sputtered region small bumps on substrate surface are visible in SEM. These bumps look like crystal ready to emerge from the substrate. See Figure 22.

If nanocrystals cover most surface segmentation classifies almost whole image belonging to only one class, seeding was noted to give this kind of images especially when sample was dragged along the bottom of seed container.

4.1.5 Other

XRD results of the scraped and reprocessed sample (s79) with nanocrystals before and after heat treatment (ultahigh vacuum heating) have significant differences as most of previously recorded peaks disappeared. Substrate peaks were acquired from

measured GaAs piece. SEM images do not show changes to nanocrystal surface texture and morphology due to heat treatment. Figure 23 shows recorded diffraction patterns for substrate and sample before and after heat treatment, common peaks between any diffraction patterns are marked to the figures. The strong substrate peaks dominate the diffraction pattern also in synthesized sample.

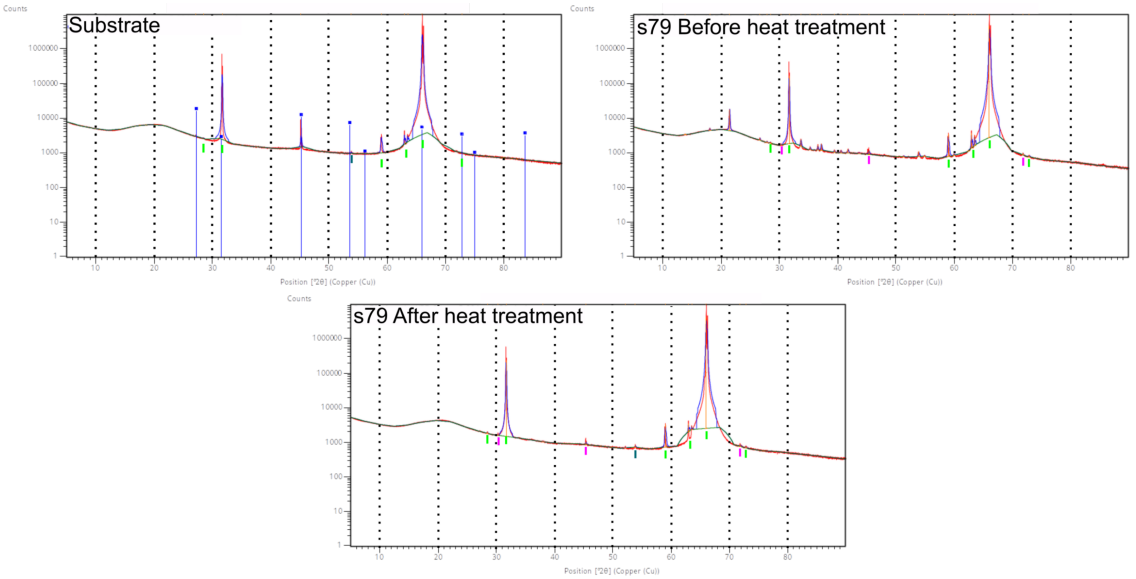

Figure 23. Measured diffraction patterns of substrate and reprocessed sample (s79) before and after heat treatment. Peaks common between measurements are marked with short coloured lines below the peak in question. The thin blue vertical lines and terminating blue squares visible in the image on top left indicate matches between the measured peaks and database entry for GaAs assigned by HighScore Plus software. Green lines are peaks observed in all three graphs, three violet marks are peaks common before and after heat treatment and the single blue-green line marks peaks common between substrate and the heat treated sample. Note that green marking at about 63° has two peaks around it, bringing the amount of peaks common for all three measurements to seven.

Dried droplets of two different seed solutions, which consist of solvent and nanocrystals scraped from the synthesized sample, on silicon show broken nanocrystals in piles, some smaller particles and some GaAs pieces. Droplets of water based seed solution stored for weeks show areas of fused particles, some odd balls fused from smaller particles and nanocrystals in piles, both broken and whole. T1 images indicate that the balls are also gallium oxyhydroxide due to having similar colour

than nanocrystals. See the Figure 24.

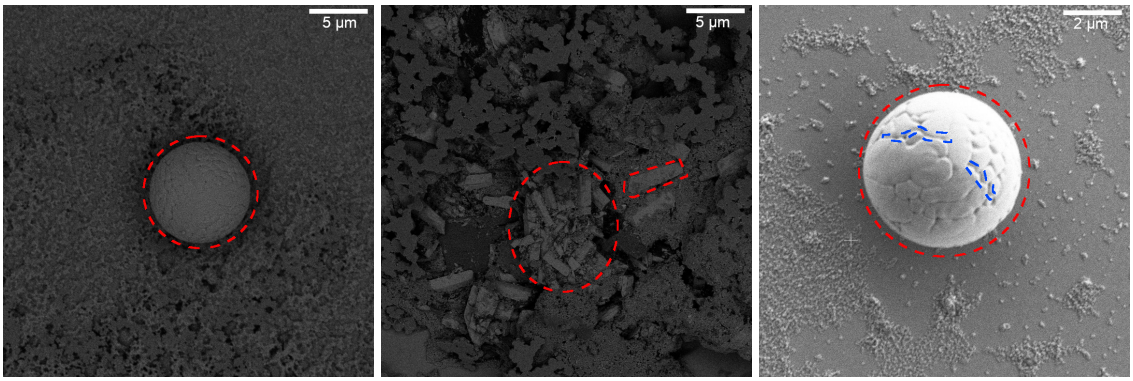

Figure 24. SEM images from drops of seed solution dried on silicon substrate. The first two from left are T1 images of one ball (red line) and nanocrystal piles. One individual nanocrystals and pile of them are marked to the second image from left with red line. On the right higher magnification ETD image of a ball showing more clearly interfaces (blue line) between particles forming the ball (red line).

Arsenic level of synthesis water diluted by factor of 120–130 was semi-qualitatively measured to be about 0,05–0,1 mg/L, so 50 mL of synthesis water contained about 0,30–0,65 mg As. The total surface area of the sample is $5{,}0\,\text{mm} * 11\,\text{mm} * 2 + 0{,}50\,\text{mm} * 11\,\text{mm} * 2 + 0{,}50\,\text{mm} * 5{,}0\,\text{mm} * 2 = 126\,\text{mm}^2$, when using 500 µm as thickness. Following numerical values are used for material properties: $\rho = 5{,}3176\,\text{g/c}^3\text{m}$, $M(Ga) = 69{,}723\,\text{g/mol}$ and $M(As) = 74{,}922\,\text{g/mol}$. Assuming that all arsenic contained in reactive surface layers of the sample is released to the water during synthesis, the lower limit thickness of reactive layer is acquired from the following calculation:

$$\frac{0{,}30\,\text{mg} * 144{,}645\,\text{g/mol}}{74{,}922\,\text{g/mol} * 5{,}3176\,\text{g/cm}^3 * 126\,\text{mm}^2} = 864\,\text{nm}.$$

The upper limit is 1,87 µm. Therefore, the reactive thickness is 0,86–1,9 µm.

4.2 Discussion

Without additional spectroscopic measurements of both sample and water at different points of time during the synthesis, it is difficult to say what reactions drive the synthesis process, but OH^- groups from water autoionization could break ionic

bonds between gallium and arsenic followed by formation of gallium hydroxide or gallium coordination complexes with either water or hydroxide. These would then break into gallium oxyhydroxide as next step.

Very thin (2–3 nm) native oxide layer does not affect to the growth of nanocrystals as it either dissolves quickly in hot water or water molecules could possibly diffuse through it, most likely both processes happen. When the thickness of the oxide layer on surface increases diffusion rate drops and time required to dissolution increases. As oxidation of the sample surface and gallium oxyhydroxide nanocrystal formation are competing processes, whether former or latter is favoured depends on multiple factors, such as temperature, pH, surface-volume ratio and thickness of non-substrate surface layer.

One potential reaction path is following $\mathrm{GaAs(s)} + 2\,\mathrm{OH^-(aq)} + 2\,\mathrm{H^+(aq)} \longrightarrow \mathrm{GaOOH(s)} + \mathrm{AsH_3(aq)}$, however this path can be expected to have at least one intermediate step likely involving gallium hydroxide or coordination complexes. The simplest first step in determining what reactions happen during the synthesis is to determine what compounds are left to the synthesis water and in what amounts.

Lattice mismatch between substrate and nanocrystal is likely cause for the tendency of nanocrystals grow at angles relative to the substrate. Width distribution of produced nanocrystals is wide with likely a peak around 700 nm. The small nanocrystals on faces of larger ones can be attributed to oriented attachment.

It seems when crystal nuclei have formed at the beginning of synthesis they become preferred attachment points where gallium hydroxides or gallium-water coordination complexes diffuse from elsewhere on the surface. This is based on the lack of very small nanocrystals on surface, which indicates that the synthesis reaction is diffusion controlled meaning that smaller particles grow faster. Ostwald ripening also might play some role in formation of the observed size distribution.

However, due to distances involved being several microns diffusion is unlikely to

be the only process involved moving precursor compounds from surface to growing crystals. One possibility is that gallium compound formed after water adsorption dissolves to the synthesis water.

Based on XPS, SEM and EDS analysis chemical roughening leads to the formation of a native oxide layer containing both gallium and arsenic oxides on the substrate surface preventing GaOOH formation either due chemical properties of this layer or possibly its thickness. The amorphous nature of this oxide layer might also prevent nanocrystal attachment. The difference between XPS results of non-synthesized (s73) and synthesized sample (s74) indicate the thickness of the existing oxide layer increases during synthesis. The used solution for chemical roughening had likely too high concentration and more dilute solution should be used to better control the roughening process.

The reflectance spectra of s82 can be attributed mainly to the thick oxide layer with small contribution from surface roughness, based on data reported by Li *et al.* [61] which shows similar reflectance curve as shown in the Figure 13 for about 100 nm thick oxide layer. The high photoluminescence is likely due to low reflectance at the excitation wavelength.

The formation of arsenic oxide nanoparticles on sample etched for 20 s is an interesting finding and likely caused by chemical properties of the surface favouring arsenic oxide particle formation or formation of arsenic rich spots during etching which are then oxidized during the synthesis step.

AFM results (Table IV) indicate that roughness after synthesis is higher than after chemical roughening but before the synthesis step. Both roughness and waviness have significantly different values at different spots on surface due to presence of holes in the oxide layer on surface and particles on edges of cracked oxide layer, other types of particles are also present on the surface. Some differences could be considered as imaging artefacts due to tip wear and other measurement imperfections, the

chosen levelling method and other processing steps also affect results.

XRD results clearly show that a phase transition from GaOOH to gallium oxide happens, however it is not possible to say that heat treated sample has α-Ga_2O_3 nanocrystals as peaks associated with it were not observed. Based on diffraction patterns of gallium oxides published previously the possibility that after heat treatment sample has transformed partially to beta gallium oxide can not be ignored. Reason for this are the missing signature peaks of alpha polymorph, that exist around 25°, 34° and 36°.

In scraped samples similar areas with no growth than those that were dragged along the bottom of the seed container are seen indicating that surface properties of these areas change so that crystal nuclei can not form. In seeded samples the small nanocrystals grow on top of normal nanocrystals, which could be explained by assuming small particles from the seed solution attach themselves to substrate and later serve nuclei for smaller nanocrystals. The increased concentration and flushing time with seed solution increase the amount of groups consisting of small nanocrystals due to more seeds attaching themselves to the substrate.

The differences between photoluminescence and reflectance of s79 and s80 are likely caused by the gallium oxyhydroxide nanocrystals covering the surface of s79 almost completely while for s80 the surface coverage is quite low with large amount of substrate surface visible. Higher surface coverage of GaOOH nanocrystals decreases reflectance and photoluminescent intensity, which indicates that carrier densities of vacancy/impurity states within bandgap where incoming photon could excite charge carrier are low compared to GaAs.

However, more likely most of the emission comes from substrate as the energy range of emission of both s79 and s80 is only slightly smaller than for s83 indicating that role of GaOOH in the photoluminescence is very small. The lower intensity noted can be explained though attenuation caused by the nanocrystals.

The excitation energy for photoluminescence measurements was about 2,3 eV, which is less than half of the bandgap of GaOOH but much larger than corresponding value (1,4 eV) for GaAs. These facts point toward surface coverage of nanocrystals as reason for the differences seen in the optical measurements (Figure 13).

The high density growth seen in the scraped and reprocessed samples is likely caused by scraping breaking the existing nanocrystals and spreading them along with gallium arsenide particles all over scraped areas. They act as attachment points or sometimes as nuclei for new nanocrystals in reprocessing.

The significantly increased surface density and smaller nanocrystals caused by adding seeds to the synthesis water are likely caused by increased gallium supply at the beginning and some seeds might acts as extra crystal nuclei. The global surface density was the highest observed during current series of experiments. However, small areas with even higher surface density are seen in some other samples due to other seeding methods but only global values are considered here. See Figures 10, 20 and 22. The low values from segmentation analysis given in the Table V are caused by smaller nanocrystal size, which decreases classification accuracy.

The lower surface density of nanocrystals and their irregular shape in sputtered samples could be caused by surface irregularities at nanoscale due to sputtering observed by Wang *et al.* [48] leading lack of attachment points at the same height level.

Therefore, nanocrystals likely attach themselves at base level not on top of the dots. As height and diameter of the dots formed during sputtering on surface vary, nanocrystals would likely preferentially form in areas with small dot heights. Other possibility is that significantly increased surface area due to sputtering favours surface oxidation reactions leading to formation oxide native layer instead of oxyhydroxide formation and diffusion to growing nanocrystals.

Thermal diffusion likely dominates surface processes when the sample is heated

during sputtering leading to much smaller surface irregularities than caused by room temperature sputtering. The role of thermal diffusion is supported by significant reduction of nanocrystal surface density on non-sputtered areas compared to baseline samples and increase of surface density of nanocrystals on areas sputtered at room temperature compared to non-heated sputtered sample.

Potential changes to the surface chemical composition due to sputtering and heating can not be ignored. Thermal conditions under sample holding clamps differ from sputtered area somewhat, which affect surface composition and texture differently compared to sputtered areas.

The large bumps observed on the surface of sputtered sample held overnight in the seed solution are likely sites where somesort nanocrystal has formed below surface and is breaking to surface. The shape and size of these areas is compatible with nanocrystal below surface.

Segmentation works well if image is high quality, has good contrast and nanocrystal distribution on surface is relatively uniform. For reliable results from segmentation based analysis averaging over multiple images with the same magnification is required. Also, a good classifier and feature combination along with fitting preprocessing method is required. Using higher pixel count images, potentially choosing higher beam energy or tilting sample could produce better images for segmentation.

In segmented T1 images tendency for misclassifying middle of nanocrystals causes issues, while in ETD images shadows are usually misclassified as belonging to crystals. Inaccuracies in segmentation based results are large, but they support the visual analysis relatively well. Segmentation does not work in images with very high degree of surface coverage.

For segmentation higher magnification images work better but suffer from surface density variation in different sites due to the tendency of the nanocrystals group together. Low magnification allows more reliable results at cost of difficulties with

the accuracy of the segmentation. Low accuracy is especially problematic with low magnification ETD images, due to low material contrast, leading to unrealistic values for surface coverage.

While low magnification images give good overview of the sample, they do not work well with segmentation due to difficulties separating neighbouring nanocrystals from each other though increasing image size could help. Averaging segmentation based results from large amount images with field of view around 60 µm will likely give the best result.

5 Conclusions

This work has demonstrated multiple ways to change surface density of GaOOH nanocrystal synthesized to surface of GaAs piece in hot water, such as roughening and seeding. The roughening caused changes could be attributed to changes in surface texture and composition affecting surface reactivity and ability of nanocrystal nuclei to form on surface.

It is clear that scraping changes either surface texture or possibly chemical properties so that growth of nanocrystals is not possible in scraped areas with former being more likely. Chemical roughening experiments showed no gallium oxide nanocrystals after synthesis likely due to changes the roughening treatment caused to the chemical composition of the surface.

The presence of arsenic oxide nanoparticles on the sample with shorter chemical roughening time could be caused by increased local arsenic concentration due to processing related events during roughening. Further testing is required to say anything definite about these arsenic oxide nanoparticles.

As sputtering decreases the surface density of the nanocrystals significantly, it could provide further clues what kind of surface treatments would be advantageous for controlling the surface density of nanocrystals. When sample is heated during sputtering thermal diffusion is likely cause for changes in the surface density of the nanocrystals.

Seeding causes local surface density changes and can be used to produce extremely high surface densities locally, but suffers from unreliability as it does not affect most of the surface. One major factor is the quality and stability of the seed solution, as the seed concentration and size distribution are unknown. This points towards extremely high concentration seed solution being advantageous, which probably should be combined with surface treatment to increase attachment probability.

To better control the seeding process methods to prepare well known seed so-

lutions has to be developed as currently the exact composition and concentration of the seed solution is unknown. This issue has ties to the harvesting problem, as harvested nanocrystals could provide the seed material.

Seeds added to the synthesis water provided the highest surface density of nanocrystals after the first synthesis round and the nanocrystals were smaller than those in the baseline samples. The noted changes to nanocrystal size and surface density could be caused by increased gallium concentration during synthesis. So in future seeding experiments other gallium compounds than gallium oxyhydroxide or arsenide, such as gallium nitrate, could be tried as gallium source. Further seeding experiments should use adding seeds to the synthesis water methodology, which seems the most promising seeding protocol.

The results of optical measurements can be explained by thick oxide layer on substrate for the chemically roughened sample and for the scraped and seeded samples though degree of surface coverage by nanocrystals.

As pH of reaction solution and possible presence of surfactants are known to affect morphology of nanocrystals synthesized with hydrothermal methods, their potential impact for this synthesis should be investigated.

Segmentation based analysis has shown its potential, but to be truly useful requires large amount high quality SEM images from every sample. Current results from segmentation were especially useful in estimating differences caused by sputtering.

Harvesting the synthesized nanocrystals intact from surface remains currently unsolved, but isotropic etching could be used especially if the etchant was good selectivity between gallium arsenide and gallium oxyhydroxide. The single attempt at chemical harvesting was inconclusive as while all nanocrystals were removed from sample surface, it is impossible to say whether nanocrystals were dissolved or not. One possible cause for this is too highly concentrated solution combined with long

etch time etching too much. Significantly more dilute solution would have smaller etch rate allowing better control over the process. Other chemical mixtures should be also evaluated.

To understand the reaction paths making the synthesis process happen, synthesis could be carried out under spectroscope. Also, composition of the synthesis water should be determined to see what reaction products have dissolved to water. Spectroscopic investigation of the substrate surface after synthesis could also provide clues of reaction paths.

Checking GaAs substrates other than (100)-orientation might give interesting results. Other compound semiconductors should be also investigated to see whether the hot water treatment would produce nanocrystals on their surface, especially gallium or arsenide based binary compound should be investigated as they could additional clues of possible reaction paths. Whether ternary compound would give nanocrystals containing both elements or only one also should be investigated.

While many issues remain unsolved regarding this synthesis method, it has provided some answers to multiple questions, such as impact of surface roughening and seeding. When looking to decrease average size of the nanocrystals and increase the amount of nanocrystals per unit area, the most fruitful approach seems to be continuing with adding gallium containing seed material to the synthesis water.

References

[1] S. I. Stepanov, V. I. Nikolaev, V. E. Bougrov, and A. E. Romanov, Rev. Adv. Mater. Sci **44**, 63 (2016).

[2] M. Kumar *et al.*, *Gallium Oxide* (Elsevier , 2019), pp. 91–115.

[3] B. Zhang, *Physical Fundamentals of Nanomaterials*, *Micro and Nano Technologies* (William Andrew Publishing Boston, 2018).

[4] S. Kumar and R. Singh, physica status solidi (RRL) – Rapid Research Letters **7**, 781 (2013).

[5] L.-C. Tien *et al.*, *Gallium Oxide* (Elsevier , 2019), pp. 67–90.

[6] B. Alhalaili, H. Mao, and S. Islam, in *Novel Nanomaterials*, edited by G. Z. Kyzas and A. C. Mitropoulos (IntechOpen Rijeka, 2018), Chap. 2.

[7] L. Qiao and M. T. Swihart, Advances in Colloid and Interface Science **244**, 199 (2017).

[8] Y.-Y. Lu, F. Liu, Z. Gu, and Z. Pan, Journal of Luminescence **131**, 2784 (2011).

[9] G. Li *et al.*, Inorg. Chem. **49**, 1449 (2010).

[10] Y. Hou, J. Zhang, Z. Ding, and L. Wu, Powder Technology **203**, 440 (2010).

[11] M. Legallais *et al.*, Solid-State Electronics **143**, 97 (2018).

[12] T. Irisawa, in *Crystal Growth Technology*, edited by K. Byrappa *et al.* (William Andrew Publishing Norwich, NY, 2003), pp. 25–54.

[13] F. Wang, V. N. Richards, S. P. Shields, and W. E. Buhro, Chem. Mater. **26**, 5 (2014).

[14] N. T. K. Thanh, N. Maclean, and S. Mahiddine, Chem. Rev. **114**, 7610 (2014).

[15] H. Fu, X. Gao, X. Zhang, and L. Ling, Crystal Growth & Design **22**, 1476 (2022).

[16] P. G. Vekilov, Nanoscale **2**, 2346 (2010).

[17] L. Jing *et al.*, Chem. Rev. **116**, 10623 (2016).

[18] P. Reiss *et al.*, Chem. Rev. **116**, 10731 (2016).

[19] J. Lee, J. Yang, S. G. Kwon, and T. Hyeon, Nature Reviews Materials **1**, 16034 (2016).

[20] L. Cormier, in *From glass to crystal: Nucleation, growth and phase separation: from research to applications* (EDP Sciences , 2021), pp. 43–66.

[21] V. I. Irzhak, Review Journal of Chemistry **6**, 370 (2016).

[22] A. V. Bandura and S. N. Lvov, Journal of Physical and Chemical Reference Data **35**, 15 (2006).

[23] H. Ibach, in *Physics of Surfaces and Interfaces* (Springer Berlin Heidelberg Berlin, Heidelberg, 2006), pp. 245–308.

[24] M. A. Henderson, Surface Science Reports **46**, 1 (2002).

[25] P. A. Thiel and T. E. Madey, Surface Science Reports **7**, 211 (1987).

[26] F. Shi and H. Qiao, Nano Select **3**, 348 (2022).

[27] S. Ge, L. Zhang, H. Jia, and Z. Zheng, Journal of Materials Research **24**, 2268 (2009).

[28] B. Alhalaili *et al.*, Sustainability **13**, (2021).

[29] D. Guo *et al.*, Materials Today Physics **11**, 100157 (2019).

[30] A. Sharma *et al.*, International Nano Letters **10**, 71 (2020).

[31] S.-J. Li, C. Zheng, and K. C. Lobring, Zeitschrift für Kristallographie - New Crystal Structures **218**, 11 (2003).

[32] J. Zhang *et al.*, APL Materials **8**, 020906 (2020).

[33] T. Wang, S. S. Farvid, M. Abulikemu, and P. V. Radovanovic, J. Am. Chem. Soc. **132**, 9250 (2010).

[34] T. Wang and P. V. Radovanovic, J. Phys. Chem. C **115**, 18473 (2011).

[35] J. Xu, W. Zheng, and F. Huang, Journal of Materials Chemistry C **7**, 8753 (2019).

[36] E. Ahmadi and Y. Oshima, Journal of Applied Physics **126**, 160901 (2019).

[37] K. Girija *et al.*, Materials Research Bulletin **48**, 2296 (2013).

[38] P. Majewski and A. Dulda, Advances in Materials Science and Engineering **2016**, 3905625 (2016).

[39] S. Ali *et al.*, Applied Catalysis B: Environmental **307**, 121149 (2022).

[40] C. Sivakumar *et al.*, Nanomaterials **11**, (2021).

[41] X. Tang *et al.*, ACS Appl. Mater. Interfaces **10**, 5519 (2018).

[42] B. Das *et al.*, Journal of Alloys and Compounds **902**, 163726 (2022).

[43] X.-S. Wang *et al.*, Acta Biomaterialia **22**, 164 (2015).

[44] J.-L. Chiang *et al.*, Materials Science and Engineering: B **276**, 115542 (2022).

[45] D. Wang *et al.*, Ceramics International **41**, 14790 (2015).

[46] C. Zeng *et al.*, Materials Research Express **8**, 055903 (2021).

[47] L. K. Ping *et al.*, Chinese Journal of Physics **73**, 195 (2021).

[48] Y. Wang, S. F. Yoon, C. Y. Ngo, and J. Ahn, Nanoscale Research Letters **2**, 504 (2007).

[49] C. Ashby, in *Properties of Gallium Arsenide (3rd Edition)*, edited by M. Brozel and G. Stillman (Institution of Engineering and Technology , 1996), pp. 703–724.

[50] J. I. Goldstein *et al.*, *Scanning Electron Microscopy and X-Ray Microanalysis*, 4th ed. 2018 ed. (Springer New York, NY, 2017).

[51] R. T. Haasch, in *Practical Materials Characterization*, edited by M. Sardela (Springer New York New York, NY, 2014), pp. 93–132.

[52] P. F. Fewster, in *X-Ray Scattering from Semiconductors (2nd Edition)* (World Scientific , 2003).

[53] A. Altomare, C. Cuocci, A. Moliterni, and R. Rizzi, in *Inorganic Micro- and Nanomaterials: Synthesis and Characterization*, edited by A. Dibenedetto and M. Aresta (De Gruyter , 2013), pp. 57–92.

[54] J. Stangl, C. Mocuta, V. Chamard, and D. Carbone, in *Nanobeam X-Ray Scattering* (John Wiley & Sons, Ltd Weinheim, GERMANY, 2013), Chap. 2, pp. 13–38.

[55] K.-W. Ng, in *Introduction to Nanoscale Science and Technology*, edited by M. Di Ventra, S. Evoy, and J. R. Heflin (Springer US Boston, MA, 2004), pp. 75–100.

[56] W. Lu and Y. Fu, in *Spectroscopy of Semiconductors: Numerical Analysis Bridging Quantum Mechanics and Experiments* (Springer International Publishing Cham, 2018), pp. 107–158.

[57] J. Schindelin *et al.*, Nature Methods **9**, 676 (2012).

[58] T. Degen *et al.*, Powder Diffraction **29**, S13–S18 (2014).

[59] I. Arganda-Carreras *et al.*, Bioinformatics **33**, 2424 (2017).

[60] X-ray Photoelectron Spectroscopy Database,Version 4.1, NIST Standard Reference Database 20, 2000, (retrieved 10.5.2022).

[61] J. Li, Y. Tian, and D. Hall, Electronics Letters **51**, 575 (2015).